

**OPTICAL-PARAMETRIC-AMPLIFICATION APPLICATIONS TO
COMPLEX IMAGES**

A Dissertation
Presented to
The Academic Faculty

by

Peter M. Vaughan

In Partial Fulfillment
of the Requirements for the Degree
Doctor of Philosophy in Physics in the
School of Physics

Georgia Institute of Technology
August 2011

**OPTICAL-PARAMETRIC-AMPLIFICATION APPLICATIONS
TO COMPLEX IMAGES**

Approved by:

Dr. Rick Trebino, Advisor
School of Physics
Georgia Institute of Technology

Dr. Kenneth Brown
School of Physics
Georgia Institute of Technology

Dr. Zhigang Jiang
School of Physics
Georgia Institute of Technology

Dr. Ali Adibi
School of Electrical and Computer
Engineering
Georgia Institute of Technology

Dr. Joseph Perry
School of Chemistry and Biochemistry
Georgia Institute of Technology

Date Approved: June 27, 2011

To my beautiful wife.

ACKNOWLEDGEMENTS

I must thank my long-term laboratory colleagues, Pamela Bowlan, Vikrant Chauhan, and Jacob Cohen, for their tireless conversations about life and science, and without whom most of this work would have surely languished incomplete. I would like to acknowledge the helpful insights of my advisor, Rick Trebino, and the direction I received from my contacts at Lockheed Martin, Del Vicker and Ed Miesak.

TABLE OF CONTENTS

ACKNOWLEDGEMENTS	iv
LIST OF FIGURES	ix
LIST OF SYMBOLS AND ABBREVIATIONS	xii
SUMMARY	xii
CHAPTER 1 : INTRODUCTION TO ULTRAFAST AND NONLINEAR OPTICS	1
1.1 Ultrafast Optical Pulses	1
1.1.1 Ultrafast Pulse Measurement	1
1.1.2 Pulse Measurement and Phase Retrieval in Ultrafast Optics	2
1.1.2.1 Frequency Resolved Optical Gating (FROG)	4
1.1.2.2 Spectral Interferometry (SI)	6
1.1.2.3 Spectral Phase Interferometry for Direct Electric-Field Reconstruction (SPIDER)	7
1.1.3 Ultrafast Pulse Generation	7
1.1.3.1 Pulse Generation from Oscillators	7
1.1.3.2 Amplification of Ultrafast Optical Pulses	9
1.2 Nonlinear Optics	11
1.2.1 Introduction to the Mathematics of Nonlinear Optics	12
1.2.2 Certain Nonlinear Interactions Explained	12
1.2.2.1 Second Harmonic Generation	12
1.2.2.2 Optical Parametric Amplification	13
1.2.2.3 Polarization Rotation	16
1.2.2.4 Supercontinuum Generation	17
1.2.3 Phase Matching in Nonlinear Optics	18

1.2.3.1 Phase Matching Bandwidth	21
1.2.3.1.1 λ -Non-Critical Phase Matching	22
1.2.3.1.2 θ -Non-Critical Phase Matching	23
1.2.3.1.3 $\theta\lambda$ -Non-Critical Phase Matching	25
CHAPTER 2 : DOUBLE-BLIND POLARIZATION GATED FREQUENCY RESOLVED OPTICAL GATING	27
2.1 Introduction	27
2.2 Single Frame Double-Blind PG FROG	28
2.2.1 Double-Blind PG FROG Experimental Configuration	30
2.2.2 Double-Blind PG FROG Experimental Parameters	32
2.3 Double-Blind PG FROG Pulse Retrieval Method	34
2.4 Experimental Results	36
2.4.1 Measurement of Two Gaussian Pulses with Differing Amounts of Chirp	37
2.4.2 Measurement of a Gaussian and a Pulse Train from an Etalon	40
2.4.3 Measurement of a Two Double Pulses	43
2.5 Conclusion	46
CHAPTER 3 : THE HISTORY OF NONLINEAR OPTICS FOR IMAGING	47
3.1 Introduction to Nonlinear Optical Imaging	47
3.2 Optical Parametric Amplification Imaging	47
3.2.1 The First Demonstration of OPA Imaging	47
3.2.2 Previous OPA Imaging of 4 lp/mm	48
3.2.3 OPA Imaging and Spatial Filtering	48
3.2.4 OPA Imaging Without Lenses	49
3.3 Sum Frequency Generation Imaging	49
3.3.1 Sum Frequency Generation of a Complex Image	49
3.4 Other Nonlinear Optical Processes for Imaging	50

3.4.1 CARS imaging	50
3.4.2 Four Wave Mixing Imaging	51
CHAPTER 4 : THEORETICAL CONSIDERATIONS FOR OPTICAL PARAMETRIC AMPLIFICATION IMAGING OF COMPLEX IMAGE-BEARING SIGNALS	52
4.1 Introduction to OPA for Complex Imaging	52
4.1.1 Laser Stability and OPA Imaging	52
4.1.2 Goals of OPA Imaging Studies	53
4.1.3 Scope of This Work in Comparison to Previous Works	54
4.2 Optimizing Gain in OPA imaging	54
4.2.1 Phase Matching Types	55
4.2.2 Limitations on Phase Matching Efficiency	55
4.3 Optical Parametric Generation	56
4.3.1 Parametric Amplification of Noise	56
4.3.2 OPA in the Presence of OPG	59
4.3.3 Gain Limitations Due to the Presence of OPG	59
4.4 Spectral Considerations for OPA Imaging	61
4.5 Maximizing Spatial Resolution in OPA imaging	63
4.5.1 Geometrical Smearing	63
4.5.2 Pump Beam Divergence	65
4.5.3 Effect of Pump Beam Spatial Profile	66
4.6 Angular Acceptance in OPA Imaging	66
CHAPTER 5 : EXPERIMENTAL DEMONSTRATIONS OF OPTICAL PARAMETRIC AMPLIFICATION IMAGING OF COMPLEX IMAGE-BEARING SIGNALS	69
5.1 Experimental Apparatus for OPA Imaging in the Fourier Plane	69
5.1.1 Vacuum Spatial Filter	69
5.1.2 Description of the Entire Apparatus	73

5.2 Experimental Results and Discussion	74
5.3 The Space-Bandwidth Product (SBP)	77
5.3.1 SBP of Our Measurement and Comparison to Previous Work	78
5.3.2 Limitations on the Measurement of the SBP	78
5.4 Conclusions	79
CHAPTER 6 : SPATIAL FILTERING DURING OPA IMAGING	81
6.1 Introduction to Image Processing	81
6.2 Real-Time Spatial Filtering as Image Processing using Nonlinear Optics	81
6.2.1 Spatial Overlap for Image Processing	81
6.2.2 Phase Matching for Image Processing	82
6.2.3 Image Processing Using the Real Image Plane Geometry	83
6.2.4 Image Processing Using the Fourier Plane Geometry	84
6.3 Theoretical Investigation of Spatial Filter Processing	85
6.3.1 Spatial Overlap of the Fourier Transform and a Gaussian Pump Beam	88
6.3.2 Spatial Overlap of the Fourier Transform and a Cylindrical Pump Beam	89
6.4 Experimental Demonstration of Spatial Filter Image Processing	91
6.4.1 Demonstration of Spatial Filtering by Pump and Seed Overlap	91
6.4.2 Demonstration of Phase Matching as a Ring-Shaped Aperture	94
APPENDIX A : THE PROOF THAT THE FOCUS OF A LENS IS THE FOURIER TRANSFORM PLANE	95
APPENDIX B : DESCRIPTION OF THE USAF 1951 TARGET	100

LIST OF FIGURES

Figure 1. Non-collinear phase matching angles in BBO.	24
Figure 2. Angle noncritical phase matching in BBO.	24
Figure 3. Single shot FROG uses transverse x position to determine delay.	29
Figure 4. The schematic of a single shot double-blind PG FROG.	31
Figure 5. Each cycle during pulse retrieval in double-blind PG FROG.	35
Figure 6. Simulated double-blind PG FROG traces and pulses.	35
Figure 7. The first of two chirped pulses measured with DB PG FROG.	38
Figure 8. The second of two chirped pulses measured with DB PG FROG.	39
Figure 9. A pulse from an etalon measured with DB PG FROG.	41
Figure 10. A simple pulse used to measure the etalon pulse with DB PG FROG.	42
Figure 11. The first of two identical double pulses measured with DB PG FROG.	44
Figure 12. The second of two double pulses measured with DB PG FROG.	45
Figure 13. A typical Fourier transform OPA imaging apparatus.	53
Figure 14. OPG rings at several different crystal angles.	58
Figure 15. OPA and OPG interfere when both processes occur simultaneously.	59
Figure 16. Wave-vector mismatch for and the OPG-ring angles.	60
Figure 17. The input spectrum and the two output spectra after the OPA.	61
Figure 18. The gain changes over the seed pulse bandwidth.	62
Figure 19. Geometrical smearing arises due to crystal thickness.	64
Figure 20. A diverging pump beam increases the point spread function.	65
Figure 21. Angular phase matching at 50% conversion efficiency.	67
Figure 22. A spatial profile cleaning pinhole system.	70
Figure 23. A very poor spatial profiles is spatially filtered.	71

Figure 24. Profiles of the pump beam both (a) before and (b) after filtering.	72
Figure 25. OPA imaging experimental apparatus.	73
Figure 26. Results of image amplification and image wavelength shifting.	75
Figure 27. An image of the USAF 1951 target and its Fourier spectrum in log scale with a simulation of the USAF 1951 target and its Fourier spectrum in log scale.	87
Figure 28. The effect of a large versus small Gaussian pump beam.	88
Figure 29. A thick, long cylindrical pump beam and a thin, short beam.	90
Figure 30. A spatially filtered USAF1951 target where horizontal features are preserved while vertical features beyond the largest are not resolvable.	93
Figure 31. A sequence of images showing the ring-shaped aperture.	94
Figure 32. The thickness of a lens depends on the transverse position across the lens.	96
Figure 33. Schematic of the USAF-1951 resolution test target.	101

LIST OF SYMBOLS AND ABBREVIATIONS

OPA	optical parametric amplification
lp/mm	line pairs per millimeter
TBP	time bandwidth product
fs	femtoseconds, or 10^{-15} seconds
$I(t)$	temporal intensity
$\phi(t)$	temporal phase
FROG	frequency resolved optical gating
SI	spectral interferometry
SPIDER	spectral phase interferometry for direct electric-field reconstruction
Ti:S	titanium-doped sapphire, a lasing medium
CW	continuous wave laser
$\chi^{(N)}$	N^{th} order nonlinear optical susceptibility
SFG	sum frequency generation
DFG	difference frequency generation
SHG	second harmonic generation
PG	polarization gating
BBO	β -barium borate, or β -BaB ₂ O ₄
DB PG FROG	double-blind polarization gating FROG
FWHM	full width at half maximum, a definition of pulse length
SBP	space bandwidth product
CARS	coherent anti-stokes Raman spectroscopy
OPG	optical parametric generation

SUMMARY

Ultrafast optical pulses have many useful features. One in particular is their ability to exploit nonlinear processes due to their extremely short durations. We have used ultrafast optical pulses, primarily focused on the nonlinear processes of Polarization Gating and of Optical Parametric Amplification, one for measurement and the other for imaging purposes. For measurement, we have demonstrated a robust method of measurement to simultaneously measure both optical pulses used in a pump-probe type configuration. In these measurements, no initial information beyond the nonlinear interaction between the pulses is required. We refer to this method of pulse measurement as Double-Blind Polarization Gating FROG[1].

We have demonstrated this single-shot method for measuring two unknown pulses using one device. We have demonstrated this technique on three separate pulse pairs. We measured two Gaussian pulses with different amounts of chirp. We measured two double pulses with different pulse separations, and we have measured two extremely different pulses, where one was simple Gaussian and the other was a pulse train produced by an etalon. This method has no non-trivial ambiguities, has a reliable algorithm, and is automatically phase matched for all spectral bandwidths. In simulations[2], this method has proven to be extremely robust, measuring very complicated pulses with TBPs of ~ 100 even in the presence of noise.

In addition to pulse measurement, we have demonstrated the processes of Optical Parametric Amplification (OPA) applicability to imaging of complex objects[3]. We have done this where the Fourier transform plane is used during the interaction. We have amplified and wavelength converted a complex image. We report imaging of spatial

features from 1.1 to 10.1 line pairs/millimeter (lp/mm) in the vertical dimension and from 2.0 to 16.0 lp/mm in the horizontal dimension. We observe a gain of ~ 100 , and, although our images were averaged over many shots, we used a single-shot geometry, capable of true single-shot OPA imaging. To our knowledge, this is the first Fourier-plane OPA imaging of more than a single spatial-frequency component of an image. We observe more than 30 distinct spatial frequency components in both our amplified image and our wavelength shifted image. The two-dimensional SBP for our Fourier-plane OPA imaging system was $\sim 46,000$.

We have demonstrated all-optical spatial filtering for these complex images[4]. We have demonstrated that direct Fourier filtering of spatial features is possible by using a shaped pump beam. We have simply used a line shaped pump beam generated by a use of cylindrical lens. Further, the phase matching leads to interesting image-processing results, which are controlled by rotation of the crystal angle. The phase matching condition acts like a ring-shaped physical aperture on the image. We can isolate certain portions of the image simply by rotating the crystal. The Fourier plane of interaction allows for both spatial-frequency and spatial-feature filtering, with wide latitude available in the spatial-frequency transfer function through the use of exotic shaped pump beams.

CHAPTER 1

INTRODUCTION TO ULTRAFAST AND NONLINEAR OPTICS

1.1 Ultrafast Optical Pulses

Ultrafast optics broadly refers to the generation and use of very short bursts of light, typically generated by specially designed lasers. These optical laser pulses can be as short as a few femtoseconds ($\sim 10^{-15}$ seconds) in duration. These pulses have found significant applications in physics, nonlinear optics, chemistry, and biology. Precise measurement of such pulses has significant difficulties.

1.1.1 Ultrafast Pulse Measurement

To understand the problem of ultrafast optical pulse measurement, we first look at the mathematical expression for an ultrafast optical pulse. This is given by

$$\mathcal{E}(t) = \frac{1}{2} \sqrt{I(t)} \exp\{i[\omega_0 t - \phi(t)]\} + c.c. \quad (1.1)$$

in which $I(t)$ is the intensity, ω_0 is the carrier frequency, $\phi(t)$ is the phase, and the $+ c.c.$ denotes that there is also a complex conjugate term. It is traditional in discussing such pulses to suppress the complex conjugate term and the fast oscillating carrier frequency and describe the pulse as

$$E(t) = \sqrt{I(t)} \exp\{-i\phi(t)\} \quad (1.2)$$

From either description (1.1) or (1.2), it is clear that a complete description of the pulse requires knowing the intensity of the pulse as well as its phase. An ultrafast pulse can equivalently be described by its spectrum and spectral phase instead of its temporal intensity and temporal phase, as there is a well-known Fourier relationship between these two descriptions

$$\tilde{E}(\omega) = \sqrt{S(\omega)} \exp\{-i\varphi(\omega)\} \quad (1.3)$$

in which we have suppressed the carrier frequency and complex conjugate term.

An ultrafast pulse will necessarily have a large spectral bandwidth because of the same Fourier relationship. The uncertainty in the temporal domain is the temporal bandwidth. The product of the uncertainty in the temporal domain with the uncertainty in the spectral domain must be at least 0.5 (depending on which precise definition of ‘width’ is used)[5]. The uncertainty in the spectral domain is the spectral bandwidth, so a short pulse must also be a broadband pulse. To measure such a pulse, a measurement scheme must have sufficient temporal resolution to resolve the fast features in time and sufficient spectral resolution to measure the fast features in frequency.

1.1.2 Pulse Measurement and Phase Retrieval in Ultrafast Optics

One basic description of ultrafast optics is the generation and use of the shortest duration events ever created by man. This is directly related to the difficulty in measuring these phenomena. In general, to measure a fast event, a stroboscopic technique is used. A significantly faster flash is used to freeze the fast action and record the event, or to record several frames in series. This method of stroboscopic study was first performed by Eadweard Muybridge in *The Horse in Motion*, where the fast moving object, a galloping horse, was studied as a series of still images[6]. Clearly, this technique cannot be performed with the fastest objects ever created, as by definition there is no faster event to use as a strobe.

While no faster event is available to use as a strobe, an ultrafast pulse is always present with an event of comparable length – a replica copy of the pulse itself which can be generated using a beam splitter. The first attempt to measure these pulses was

intensity autocorrelation[7], where the intensity from a nonlinear interaction (which only occurs when both replicas of the pulse are present simultaneously) is recorded. One of the copies of the pulse is temporally scanned, so that the nonlinear intensity can be recorded as a function of time. While the intensity autocorrelation does give an approximation to the pulse length, it does not contain sufficient information to actually determine the duration of the pulse.

Because there is no fast strobe available to measure ultrafast optical pulses, the intensity versus time cannot be frozen, as happens with flash photography or stroboscopy. It is therefore important, referring to (1.2), to measure not just the intensity, $I(t)$, but also the phase, $\phi(t)$. The importance of the phase of an ultrafast pulse can best be understood by considering the frequency components of the pulse. The phase describes the relative arrival times of the frequency components of the pulse. Thus when a pulse has a flat phase, the frequency components of the pulse all arrive simultaneously. A flat phase pulse will have the shortest temporal duration. Two pulses may have identical spectra, but the pulse with non-simultaneous frequency components (which will have a non-linear phase), will clearly be longer in duration than a pulse whose frequency components are temporally coincident. From this, it is clear that the intensity alone is insufficient information to determine the duration of the pulse, and phase retrieval is a required component of pulse measurement.

Direct phase measurement is impossible since the complete field (1.2) is a complex quantity. Physical detectors are only capable of measuring real quantities. All detectors record intensities, such as the spectrum measured with a spectrometer or the temporal intensity with a photodiode and an oscilloscope. The one-dimensional phase

retrieval problem is mathematically impossible to solve[6] so that a measurement only of the spectrum cannot reveal phase information or measurement only of the temporal intensity cannot yield the phase information. However, the two-dimensional phase retrieval problem can be solved in certain circumstances[8], and two-dimensional phase retrieval methods are commonly used to characterize ultrafast optical pulses.

As we have stated, ultrafast optical measurement involves measuring an event without the possibility of using a shorter event during the measurement. Ultrafast optical measurements almost universally utilize an interaction between the pulse and a replica of the pulse itself[9]. A semi-reflective optic such as a beam-splitter can be used to generate the two pulse replicas.

1.1.2.1 Frequency Resolved Optical Gating (FROG)

The most successful technique for complete retrieval of the intensity and phase where initially nothing is known about the pulse is Frequency Resolved Optical Gating (FROG)[6]. The FROG technique is a measurement technique which uses two dimensions of information, frequency and delay, so that the problem becomes a two-dimensional phase retrieval problem. It uses an experimental configuration which has sufficient constraints to yield an essentially unambiguous solution. The only ambiguities in FROG which have been found are the so-called trivial ambiguities[10-12], such as the absolute phase of the pulse, the arrival time of the pulse at the detector and the phase relationship between two pulses which for which there is zero intensity between the peaks.

FROG measurements involve the generation of a FROG trace, which is simply a spectrally resolved autocorrelation. This measurement is done by generating an

instantaneous nonlinear interaction of any type between the two pulse replicas, so long as the mathematical form of the interaction is well defined. The output from the nonlinear interaction is then sent into a spectrometer and the spectrum is recorded, yielding one of the two dimensions of information needed for phase retrieval. One of the two replicas is then delayed with respect to the other. As each delay, a spectrum is taken. The delay is scanned from a time where one of the pulses is so far ahead of the other that there is no nonlinear interaction until that pulse is so far behind the other replica that there again is no interaction. The delay steps are controlled so that there is a known, fixed delay between each measurement. Mathematically, the FROG trace is given by

$$I(\omega, \tau) = \left| \int E(t) g(t - \tau) e^{-i\omega t} dt \right|^2 \quad (1.4)$$

where it is the form of the nonlinear interaction which determines the gating function $g(t - \tau)$.

Such a map of delay time versus spectrum is similar to a spectrogram, although the mathematical form of the spectrogram involves the assumption that the gate pulse is known, whereas in FROG the gate pulse is some nonlinear function involving the pulse to be measured itself. The most commonly encountered spectrogram is a musical score, where notes (frequency) are mapped versus time (delay). In the same way that a musical score completely determines the piece of music played, the spectrogram completely determines the complex electric field (1.2).

The actual retrieval of the pulse field from the spectrogram involves using a two-dimensional phase-retrieval algorithm. The General Projections[13] algorithm is commonly used in FROG measurements, and is the reason the mathematical form of the interaction must be known. To perform this retrieval, a random guess for the pulse is

initially made, and the spectrogram of that pulse is calculated. The pulse is then changed to be something which satisfies the mathematical constraint of the form of the nonlinear interaction. A new spectrogram is calculated, which is closer in actuality (determined by RMS error, commonly called the G-error) to the original measured trace. Then a new pulse is generated which has the same trace as that of the measured pulse (which is referred to as the data constraint). This pulse is then changed to satisfy the mathematical constraint again. Through this iterative process, a pulse which satisfied the mathematical constraint of the nonlinear interaction and which also generates the measured spectrogram is generated.

1.1.2.2 Spectral Interferometry (SI)

Spectral Interferometry is another method for recovering the complete electric field of an unknown pulse exploiting information from both the frequency and time dimensions. This method is a linear technique, so pulses which are too weak to initiate nonlinear processes can be measured using SI. To perform a SI measurement, one of the two input pulses must be known, perhaps by having measured it using FROG, where no previously characterized pulse is required. Two separate pulses, the known pulse and the unknown pulse, are made to collinearly impinge upon a spectrometer. If there is a delay between the peaks in the intensities of these pulses, there will be spectral interference measured at the spectrometer. Then, so long as the spectra of the unknown pulse is completely encompassed by the spectra of the known pulses, all of the information about the unknown pulse is present in the interference. SI is an extremely powerful pulse measurement technique provided that the experimenter has a previously characterized reference pulse with a spectrum that encompasses the unknown pulse spectrum.

1.1.2.3 Spectral Phase Interferometry for Direct Electric-Field Reconstruction (SPIDER)

SPIDER is another common pulse measurement method. It involves the use of spectral-shear interferometry. One of the pulses to be measured is sent through a pulse stretcher[14] and is chirped, so that its more red frequencies temporally lead its bluer frequencies. The other replica is passed through a Michelson interferometer[15], generating a double pulse[16]. The two pulses are then nonlinearly mixed to generate a sum-frequency signal. The sum-frequency output is sent into a spectrometer, and spectral fringes are seen because of the interference between the delayed peaks in the double pulse. As each of these peaks interacted with a different frequency component of the chirped pulse, the interference fringes contain all of the information about the initial pulse.

SPIDER is advantageous in that there is a direct inversion algorithm between the measured spectrum and the initial input pulse, so retrieval can be much faster than iterative phase retrieval processes such as FROG. However, SPIDER is experimentally difficult, and small calibration errors in the pulse chirp or in the double pulse spacing can lead to large errors in the measurement[9, 17]. Further, because the only measured value is the spectrometer signal, only one measurement has taken place and so there is no way to determine if a SPIDER calibration error has occurred.

1.1.3 Ultrafast Pulse Generation

1.1.3.1 Pulse Generation from Oscillators

The generation of ultrafast pulses is also a nontrivial problem. Pulsed lasers can be realized using many different types of lasing media: gases such as CO₂, semiconductors such as titanium doped sapphire (Ti:S), or dyes such as Rhodamine or

Malachite green. The simplest form of a pulsed laser is an electronically switched pulsed laser. In these systems, a continuous wave (CW) laser is sent through an electrically controlled shutter. Such systems have pulse durations limited by the electronic response of the shutter, and generally have pulse durations as short as 10 nanoseconds (ns). Such pulses, however, are not considered ultrafast pulses. One characteristic of ultrafast pulses is the use of mode-locking[8].

One method of taking a long pulse laser and making it into an ultrafast laser is to use a saturable absorber[5]. Such a medium has an intensity dependant absorption which has a peak below the peak of the laser intensity. As a result, when the long pulse passes through such a medium, the leading weak edge is absorbed, shortening the pulse.

Absorption continues until the saturation level is reached. Passing a pulse through such a medium several times can compress a long pulse into a pulse as short as 500 fs.

Saturable absorbers are one method of passive mode-locking. This is one method of generating pulses in the ultrafast regime, but the absorber limits both duration of the output pulses and their intensity.

The standard method of generating ultrafast optical pulses, with durations as short as a single optical cycle, is Kerr-lens mode-locking[18, 19]. This is the mechanism for pulse generation used in Ti:S oscillators, and is the method used for generation of ultrafast optical pulses described in this thesis. Ti:S lases both in CW and in a pulsed mode. In an oscillator, these two methods of lasing compete for energy. Because Kerr lensing is a non-linear effect, it is intensity dependant. Essentially, when light is present in a medium, the index of refraction of the medium is modified to cause the light to focus. A more intense beam will focus more than a less intense beam. Because a short

pulse is more intense than a long pulse, the short pulse will experience this effect more than the CW pulse. To generate pulsed outputs from a Ti:S cavity, curved mirrors are placed around the lasing medium, which also happens to be the medium where the Kerr lensing effect occurs, and these curved mirrors are designed to re-collimate the focused light. In this manner, the short pulses of light which had focused at the crystal propagate in a collimated fashion through the cavity, while the CW light is made to diverge by the optics which collimate the pulses.

Ti:S oscillators are widely used in ultrafast optics because of their simplicity of maintenance and their tunability[20]. Such laser can be tuned to have center wavelength anywhere from 700nm-1000nm, spectral bandwidth between 10nm and 90nm, and durations from 2fs-500fs. These systems typically produce pulses at 80Mhz with average power of 500mW. As a result, such pulses have energies of 1-10nJ per pulse, and peak intensities between 2kW and 5MW[21].

1.1.3.2 Amplification of Ultrafast Optical Pulses

Nonlinear optical effects are generally intensity dependant. As a result, amplification of the peak power of ultrafast pulses results in more readily accessible nonlinear interactions. The most common method of amplification for ultrafast optical pulses is Regenerative Chirped Pulse Amplification[22]. This amplification scheme is referred to as CPA, and such an amplifier system is referred to as a regen.

Ultrafast pulses cannot be amplified directly. The purpose of amplifying such pulses is to perform nonlinear optical experiments, but amplifying a short pulse will result in having intensity well above the damage threshold of some optical component in

the amplifier system. The component with the lowest damage threshold is typically the gain medium, and damaging this is clearly something which must be avoided.

All regenerative amplifier systems are preceded by optical stretchers[23]. A stretcher is an optical system consisting of four dispersive elements, typically gratings. These can be designed with a single dispersive element which is passed through four times[24]. The angular dispersion from the first two passes through the dispersive element cause the pulse to be collimated with a large footprint, with the red colors on one side of the beam and the blue colors on the other side of the beam. The next two passes cause the spatial footprint to again be made small, but now with the red colors temporally leading the blue colors. Such pulses are not short, but instead display a massive amount of chirp, hence the name Regenerative Chirped Pulse Amplification. Such stretching systems can increase the duration of the pulse by as much as 5 orders of magnitude in duration.

This long chirped pulse then undergoes amplification. Since it is no longer short, the peak intensity of the chirped pulse is much less than the peak intensity would be for a non-chirped pulse. In fact, all such amplifier systems detect the pulse during the stretching process and automatically shut off if the pulse shows an insufficient amount of chirp in order to avoid damage to the optical components of the amplifier cavity.

Amplification occurs in a cavity, which is why it is referred to as regenerative. The wave polarization determines whether it oscillates through the cavity or is rejected before amplification occurs. Ultrafast Ti:S oscillators generate pulses which are p-polarized. The first optic in a regen is a thin film polarizer, used in such a configuration that a s-polarized pulse will enter the cavity and a p-polarized pulse will be rejected. A

Pockels' Cell is a transparent crystal which acts as a wave plate when a proper voltage is applied across, so that when the pulse enters the Pockels' Cell while the voltage is being applied, the pulse rotates its polarization. One incoming stretched pulse thereby has its polarization rotated, so that it becomes trapped in the cavity. The gain medium of the cavity is externally pumped, and the stretched pulse receives energy from the external pump source. Once maximal gain has been achieved, a second Pockels' Cell is activated, and the pulse is rejected from the cavity. This rejected path is separate from the rejected path of an unamplified pulse, so that the amplified stretched pulse can be isolated.

Lastly, the chirp must be removed. This is performed in a device called a compressor, which is designed to undo the effects of the stretcher[25]. The compressor is one of the limiting factors on the energy available from a regen system. As the pulse is compressed by using four passes from a grating, the damage threshold of the optics in the compressor must not be exceeded. Further, gratings are only about 80% efficient, so significant losses occur during the four grating passes. However, even with these losses, the output from a regen is typically about 1mJ, roughly five orders of magnitude greater than the oscillator 10nJ per pulse energy levels. However, the average power of such amplifier systems is still comparable to the average power from oscillators because regen systems typically operate at a repetition rate of 1kHz. For nonlinear experiments, it is the peak power of a single pulse which is important, not the average power of the laser.

1.2 Nonlinear Optics

This dissertation work requires several nonlinear optical processes to occur. We make extensive use of the processes of second harmonic generation, difference frequency generation, polarization rotation, and supercontinuum generation. Because of the

importance of these processes to this work, we will review nonlinear optics, and specifically these processes.

1.2.1 Introduction to the Mathematics of Nonlinear Optics

In linear optics, the principle of superposition dictates that when two or more waves are simultaneously present in a medium, their instantaneous intensities will add together to yield the effective intensity. As the waves move apart, each will retain its original form. While the waves are able to constructively or destructively interfere, there is no exchange of energy between the waves in linear optics.

All nonlinear optical processes are results of supplying input fields into the wave equations and looking at the polarization beyond the linear approximation. The wave equation beyond the linear term is simply:

$$\nabla^2 E - \frac{n^2}{c^2} \frac{\partial^2 E}{\partial t^2} = \frac{4\pi}{c^2} \frac{\partial^2 P^{NL}}{\partial t^2} \quad (1.5)$$

The supplied electric field is the sum of two input fields:

$$E(t) = A_1 e^{-i(\omega_1 t - \vec{k}_1 \cdot \vec{r}_1)} + A_2 e^{-i(\omega_2 t - \vec{k}_2 \cdot \vec{r}_2)} + \text{c.c.} \quad (1.6)$$

Here, the A_i are the complex amplitudes of the fields, and P_{NL} is the polarization field for all terms beyond the first term in a Taylor expansion of the field. During the nonlinear interaction, we the beams are considered as interacting photons, the Manley-Rowe relations[26] dictate that momentum and energy must be conserved for the individual interacting photons.

$$\hbar \vec{k}_1 \pm \hbar \vec{k}_2 = \hbar \vec{k}_3 \quad (1.7)$$

$$\hbar \omega_1 \pm \hbar \omega_2 = \hbar \omega_3 \quad (1.8)$$

1.2.2 Certain Nonlinear Interactions Explained

1.2.2.1 Second Harmonic Generation

The mixing of a pair of wave to produce a third wave is a second order process. In order for this to occur, the material must be anisotropic, that is $\chi^{(2)}$ must not vanish. There are only two second order processes which can occur. The two input frequencies can add together to perform Sum Frequency Generation (SFG) where the sign in (1.8) is positive or the lower frequency can be subtracted from the higher frequency to perform Difference Frequency Generation (DFG) where the sign in (1.8) is negative.

Second Harmonic Generation (SHG) is a special case of SFG. In SHG, there is only a single input wave, and it supplies both photons for the nonlinear interaction. The nonlinear polarization in (1.5) is $P^{NL}(\omega + \omega = 2\omega) = 2\chi^{(2)}E_1E_1$. Experimentally, this process is easily accessible because with only a single beam interacting with itself, the two input beams are always collinear.

Frequently, FROG is performed using degenerate SFG, which is incorrectly referred to as SHG FROG. In degenerate SFG, the input beams are at the same frequency, but are not collinear. A beam splitter (or in the case of GRENOUILLE a Fresnel biprism[27]) creates two replicas of the beam. These replicas are sent through a nonlinear medium and made to cross at an angle so that single shot FROG can be performed (see section 2.2). While degenerate SFG has the same symmetric properties of SHG FROG[28], it does not technically use the Second Harmonic Generation process.

1.2.2.2 Optical Parametric Amplification

The process of Optical Parametric Amplification (OPA) is a special case of DFG. It involves mixing two waves which are referred to as the pump and signal beams, and the generation of a third wave, which is called the idler beam. OPA has two main

functions, and because the desired output from each function is at a different wavelength, the nomenclature of OPA is ambiguous, although in all OPA interactions the pump beam is always contains the most power and it always at the highest frequency. Some literature refers to the signal beam as the wavelength which is supplied along with the pump beam and the idler as the generated wavelength for conservation of energy to hold true. This is common in experiments where the amplification is the sought after feature of the interaction, and the amplified signal wave is the one which is studied after the interaction. However, when the wavelength shifting features of the energy conservation is of interest, the term ‘signal’ refers to the lower wavelength of the two non-pump beams and ‘idler’ refers to the shorter wavelength output from the interaction. To avoid this confusion, we will avoid the ‘signal’ and ‘idler’ nomenclature. We will refer to the pump wave as the pump, the supplied wave which is not the pump as the ‘seed’, the output of the experiment at the same wavelength as the seed as the ‘OPA beam’ and the wavelength converted output as the ‘DFG beam’.

This process is a special case of the nonlinear process of DFG. In DFG, two waves are supplied with approximately equal amplitudes, and a third wave is generated at the frequency which is the difference between the two supplied waves, as determined by (1.8). In the special case of OPA, the beam at the highest frequency, the pump beam, is very intense and the beam at the lower frequency supplied wave, the seed beam, is relatively weak. The process then leads to exponential gain in the weak seed beam as well as the generation and subsequent amplification of the generated energy conserving beam.

For DFG, the nonlinear polarization in (1.5) is $P^{NL}(\omega_p - \omega_s) = 2\chi^{(2)}E_1E_2^*$. The unique role which OPA plays in nonlinear optics arises when DFG occurs and the pump frequency is the lowest. As a result, in the quantum mechanical picture, a pump photon is destroyed to generate both a signal photon and an idler photon, while still satisfying energy conservation.

The OPA beam, DFG beam, and pump beam will be coupled. How these beams interact arises from the wave equation and an application of the Slowly Varying Envelope Approximation, which states that the wavelength is much shorter the wave packet, or alternatively stated that the wave-packet contains many cycles. When single cycle pulses are used for the pump or seed beam, this approximation may be simply removed.

Because the imaging portions of this dissertation all rely on properties of OPA, we will here lay out the mathematics behind this process. When all of the beams propagate in the z direction, the coupled Amplitude Equations are:

$$\begin{aligned}\frac{dA_{OPA}}{dz} &= Q \frac{\omega_{OPA}^2}{k_{OPA}} A_{PUMP} A_{DFG}^* e^{i\Delta kz} \\ \frac{dA_{DFG}}{dz} &= Q \frac{\omega_{DFG}^2}{k_{DFG}} A_{PUMP} A_{OPA}^* e^{i\Delta kz}\end{aligned}\tag{1.9}$$

where $\Delta k = k_{PUMP} - k_{OPA} - k_{DFG}$ is the phase mismatch and $Q = 8\pi i d_{eff} / c^2$.

The solutions to these coupled wave equations are

$$A_{OPA}(z) = \left[A_{OPA}(0) \left(\cosh gz - \frac{i\Delta k}{2g} \sinh gz \right) + \frac{\kappa_{OPA}}{g} A_{DFG}^*(0) \sinh gz \right] e^{i\Delta kz/2}\tag{1.10}$$

$$A_{DFG}(z) = \left[A_{DFG}(0) \left(\cosh gz - \frac{i\Delta k}{2g} \sinh gz \right) + \frac{\kappa_{DFG}}{g} A_{OPA}^*(0) \sinh gz \right] e^{i\Delta kz/2}\tag{1.11}$$

where $g = \left[\kappa_{OPA} \kappa_{DFG}^* - \left(\frac{\Delta k}{2} \right)^2 \right]^{1/2}$ is the gain factor and $\kappa_j = Q \frac{\omega_j^2}{k_j} A_{PUMP}$.

As can be seen from the solutions for the coupled waves, there are outputs at two separate frequencies. In our considerations $A_{OPA}(0)$ is non-zero and $A_{DFG}(0)$ is zero, so from (1.10), the output beam and the same frequency as the input, the OPA beam, grow hyperbolic cosine. Equation (1.11) shows that the wave which is not supplied grows as hyperbolic sine. Therefore, both outputs grow exponentially in the intensity of the pump beam. The DFG beam which is generated also displays exponential growth once it has been generated. However, since there is no DFG beam photon present in the beginning of the interaction, the gain in the idler is technically infinite.

1.2.2.3 Polarization Rotation

A third order effect involves the mixing of three waves, and one useful third order effect is Polarization Rotation, the nonlinear process which Polarization Gating FROG (see section 2.1) relies on. The three inputs beams in a third order process do not have to be separate beams, just as Second Harmonic Generation (section 1.2.2.1) uses a single beam for both of the interacting waves. Polarization rotation occurs when two of the interacting beams are the same. If we call the two interacting beams wave 1 and wave 2, the nonlinear polarization in (1.5) becomes

$$P^{NL} = \frac{3}{4} \epsilon_0 \chi^{(3)} E_1 |E_2|^2 e^{i(\omega_1 - \bar{k}_1 \cdot \vec{r})} \quad (1.12)$$

In this case, the output beam has the same frequency as the wave 1 and also travels in the direction of wave 1. This beam can be different from wave 1, however, because it has experienced this interaction with the magnitude squared of wave 2, as shown in equation (1.12). This is the interaction which leads to polarization rotation.

Wave 2 is actually two beams which are almost identical except for their polarizations, which are orthogonal. This can be easily performed experimentally by putting in a quarter wave plate into the beam path, since a wave at 45° is made of 50% a horizontal polarized beam and 50% a vertically polarized beam. These two waves interact to generate a beam which propagates in the direction of wave 1 and has the frequency of wave 1, but which is polarized at 90° relative to wave 1. Therefore, placing a crossed polarizer relative to wave 1 in the path of the generated beam (and wave 1) should let no light through, unless there is this generated beam. This beam is not blocked by the polarizer. In this manner, a beam which experienced a nonlinear interaction can be isolated. This is how PG FROG is performed[6], and this is the nonlinear interaction we exploit to perform Double-Blind PG FROG (section 2.1).

1.2.2.4 Supercontinuum Generation

Another nonlinear process we have made extensive use of is supercontinuum generation. Supercontinuum is one of the most difficult nonlinear processes to understand because it is the result of several separate nonlinear interaction, instead of a single interaction. Because the mechanics of supercontinuum generation are beyond the scope of this dissertation, we will here only describe physically the conditions which must be met in order to generate these nonlinear effects and the output pulses which are thusly generated.

Supercontinuum generation refers to the generation of an extremely broadband pulse from an initially narrowband pulse. While we have described the ~ 50 fs pulses from our amplifier system as broadband, these pulses typically carry a bandwidth of ~ 25 nm. Supercontinuum can have a bandwidth greater than 1000nm[29]. Normally,

because supercontinuum is not transform limited, these pulses are not sub-femtosecond, but have a complex temporal and spectral structure[30]. The primary mechanisms for this are self-phase modulation and four-wave mixing. The results of supercontinuum, however, for the processes we used do not depend on the minutiae of the generation process.

In bulk materials, such as fused silica, supercontinuum generation can be used as a stable source of light over a broad range of wavelengths. The power of the continuum just above the threshold for generation can be made stable by continuously moving the bulk material using an automated translation stage, which eliminates any thermal effects. Therefore, we could use a beam focused through fused silica glass and a band pass filter to generate an infrared seed beam for our imaging applications (see section 5.1), and this infrared beam would be temporally coincident with the laser output.

Supercontinuum can be generated in many bulk materials, but can also be generated in gases. One such gas is nitrogen, and with an intense enough beam, this interaction will occur at atmospheric pressures[31]. The 800nm output from our amplifier system has sufficient power to stimulate this interaction. As a result, any time the beam was focused, the focus had to be maintained in a vacuum of at most 10 Torr in order to prevent the nonlinear breakdown of the air, and the filamentation of the beam. As a result, our spatial filter (section 5.1.1) was maintained in a vacuum chamber.

1.2.3 Phase Matching in Nonlinear Optics

One important issue which must be addressed whenever nonlinear processes take place is phase matching. Phase matching is the nonlinear optical term to describe conservation of momentum. The quantum mechanical momentum of a photon, $\hbar\vec{k}$, is

related to the wave vector \vec{k} which appears in the phase of an optical wave (see (1.6)). The two major factors which dictate phase matching conditions are the polarizations of the interacting waves and selection of the appropriate nonlinear optical crystal.

Birefringent crystals have different indices of refraction for different wave polarizations, so the wave vector can be tuned by exploiting a medium's birefringence. To see how this process works, we examine the phase matching condition by applying the plane-wave decomposition for each beam. Using Fourier decomposition, each beam in the interaction can be thought of as a plane wave. The interactions between these plane waves can be examined to approximate how the beams interact in total. The center wavelength of an ultrafast pulse is generally the only one which is considered in a plane-wave approximation.

Phase matching requires that (1.7) is satisfied, where the sign is determined by which interaction is taking place. Because $\vec{k} = (n\omega/c)\hat{s}$, the phase matching equation becomes

$$n_1\omega_1 \pm n_2\omega_2 = n_3\omega_3 \quad (1.13)$$

The index of refraction for each beam depends on several factors, including the incidence angle of the beams relative to the crystal axes, the propagation directions within the crystal, and the polarizations of each beam in a birefringent medium, and the temperature of the medium. When a non-collinear geometry is utilized, the beams do not travel in the same direction through the medium. Thus, the propagation direction through the crystal must be accounted for. This makes the problem more complicated. When using a collinear geometry, only the incidence angle into the crystal plays a role, and this can be taken care of by having the nonlinear crystal cut at the appropriate angle.

The reason that phase matching is of such critical importance in nonlinear optics can be understood by considering dispersion. In nonlinear optics, energy is shared among multiple waves and the interacting waves are at multiple frequencies. Dispersion will cause the waves to travel through the nonlinear medium at different speeds. The interactions will only take place until the waves physically separate because of dispersion. However, birefringent optical media will have waves with one polarization travel at one speed while waves with the opposite polarization will travel with another speed. Selecting the polarization of the waves and their direction of travel, the waves can be made to move the same speed through the medium. This significantly increases the interaction length between the waves, and drastically increases the output power achievable after such an interaction. The first experimental demonstration of nonlinear optics was not phase matched well[19], and the output was so weak that an editor at Physical Review removed the output spot from the plot, thinking that it was a dust particle on the manuscript[18]. Achieving significant output power from nonlinear interactions requires phase matching.

The nonlinear medium primarily used in this work was β -barium borate (β -BaB₂O₄) commonly referred to as BBO[32]. BBO is a negative uniaxial crystal, meaning that there is one birefringent axis and that the extraordinarily polarized wave will experience a lower index of refraction than the ordinarily polarized wave. The temperature dependence of the index of refraction is negligible for BBO, so that only the angle of the incident beams onto the medium, measured relative to the optic axis, determines the speed of both the ordinary and extraordinary waves through the medium[33].

1.2.3.1 Phase Matching Bandwidth

For a properly selected crystal and with properly selected wave polarizations, phase matching will occur perfectly for the center wavelength of a pulse. As was discussed in 1.1.1, an ultrashort pulse is also a broadband pulse, so that it will have large spectral frequency content. As a result, while the central wavelength will be ideally phase matched, the neighboring wavelengths will not. The amount of bandwidth that can be phase matched is related to the eventually splitting of the two pulses as they travel through the medium. There is a length over which the two pulses will continue to overlap to a certain degree. This length depends on the bandwidth of the pulses. Considering this from a different perspective, a particular nonlinear medium will be able to phase match a particular amount of bandwidth around a pair of center wavelengths. Matching the length of the medium to this coherence length of the interacting pulses ensures maximum energy transfer among the interacting beams.

“Broadband” when we discuss ultrafast pulses used for imaging has two definitions. There is the traditional definition of broadband, in that such pulses will have a large spread of wavelength content. However, when performing imaging, and especially when we perform imaging on complex objects, the pulse also carries a large wave-vector content, and this is another meaning of broadband. Using the definition of the wave vector $\vec{k} = (n\omega/c)\hat{s}$, a broadband pulse with a large spectral frequency content will contain a spread of ω , so that there will be a spread to the lengths of the wave vectors in the pulse. A broadband pulse with a large spatial frequency content, such as an image, will have a range of propagation directions. Because n and c are fixed for propagation

through a given medium, ultrafast pulses carrying images are the most broadband objects which can be made in terms of having a spread of wave vectors.

Phase matching must be accounted for in both senses of the definition of broadband in order to phase match an ultrafast image bearing seed beam. The spatial frequency case requires that a change in the incoming angles of beams not change the phase matching condition, so that $\partial \vec{k} / \partial \theta = 0$. This is referred to as “ θ -Non-Critical” phase matching. In order to phase matching the spectrum, a change of the frequency, or equivalently a change of the wavelength, needs to not alter the phase matching, so that $\partial \vec{k} / \partial \lambda = 0$, which is referred to as “ λ -Non-Critical” phase matching. While it is mathematically possible for \vec{k} , which is a function of both the angle and the wavelength, to have simultaneously vanishing derivatives with respect to both variables, this has not been found to physically occur for known nonlinear materials, according to Lantz, et al[34].

The non-occurrence of “ $\theta\lambda$ -Non-Critical” means that both the spectroscopy and the imaging cannot be performed utilizing the same phase matching method, and that perfect broadband phase matching cannot simultaneously occur for both meanings of the term. We will look at how to achieve phase matching in each separate case in order to determine the best scheme for phase matching a broadband image bearing beam.

1.2.3.1.1 λ -Non-Critical Phase matching

Wavelength non-critical phase matching requires that a change in wavelength not cause a change in index of refraction. In order to determine broadband spectral phase matching conditions, numerical calculations must be performed on the Sellmeier equations for a given nonlinear medium. Phase matching curves will change as the angle

between the pump beam and the signal beam in the medium change, which is referred to as non-collinear propagation. For a given crossing angle and nonlinear medium with a known Sellmeier equation, as well as a for a specific pump wavelength, the index of refraction change around a certain signal wavelength range can be numerically determined. An example of BBO pumped with 400nm is given in Figure 1.

The region where a change in wavelength does not result in a change in the phase matching curve can be seen from this graphic. With a non-collinear crossing angle of about 3.7° , a BBO crystal cut at slightly less than 32° will be able to phase match several hundred nanometers of bandwidth centered on 700nm.

1.2.3.1.2 θ -Non-Critical Phase matching

Using a crystal cut at a specific angle so that the beam propagation relative to the crystal axes determines the index of refraction is called critical phase matching because the directions are critical to the process. Therefore, the crystal angle cannot be used to perform θ -Non-Critical Phase matching.

Angle non-critical phase matching is most commonly done by temperature control of the nonlinear medium. Temperature dependent phase matching curves are can be found for many common nonlinear media. A potential alternative to this broadband phase matching is to utilize angle dithering of the nonlinear medium. This process involves physically rotating the crystal through a small range of angles, so that separate shots in the collected image phase match at slightly different angles. Then as the image is collected over several shots, each spatial frequency is matched at some point in the image integration.

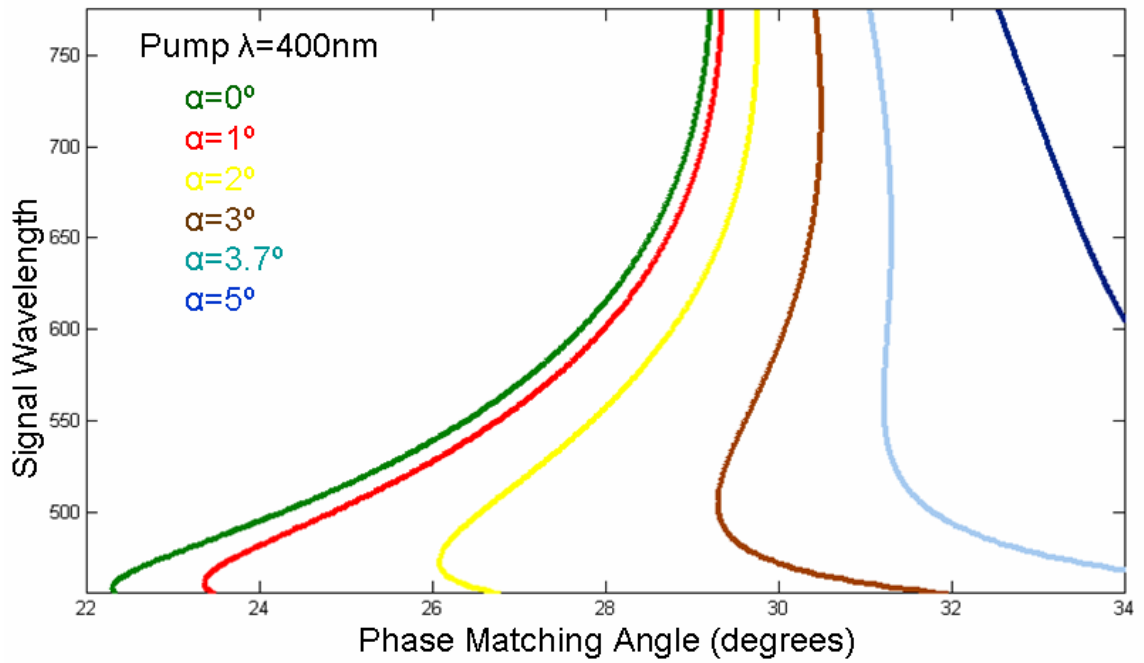


Figure 1. Non-collinear phase matching angles in BBO.

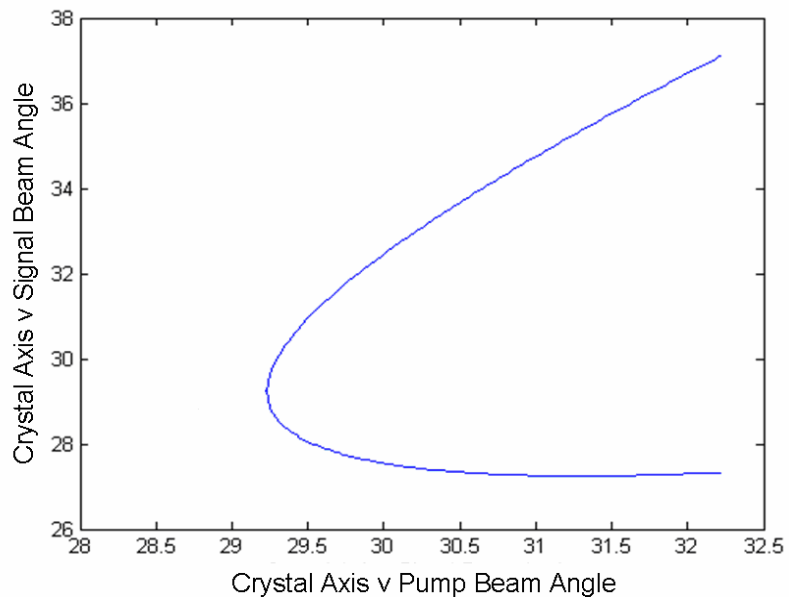


Figure 2. Angle noncritical phase matching in BBO.

The index of refraction is a function of both the wavelength and the wave vector, and it is possible for a multi-variable function to have simultaneously vanishing derivatives. A study into multi-variable phase matching away from degeneracy (where a frequency shift may occur) has never been undertaken.

For polychromatic signal amplification, the wavelength phase matching condition must be met, and has been studied extensively. For image amplification, the wave vector phase matching condition must hold, and it has been studied in less depth than its wavelength counterpart. A plot of the index of refraction on the axes of the crystal axis against signal beam propagation angle and a plot of the crystal axis against the pump beam propagation angle is the best method for visualizing this condition. The goal is to have a single pump propagation direction which will correspond to a large spread of signal propagation directions, so that many signal wave vectors can be simultaneously phase matched. This will be a vertical asymptote in the curve described above.

1.2.3.1.3 $\theta\lambda$ -Non-Critical Phase matching

A trade-off is necessary when performing both θ -Non-Critical phase matching and λ -Non-Critical at the same time. In BBO we must use the angle of the pump beam to determine the amount of spectral bandwidth we can phase match, and the angle of the pump beam and the signal beam versus the crystal axis determine the amount of angular spread in the signal that can be phase matched. For imaging, the θ -Non-Critical component is more critical, and it limits the λ -Non-Critical aspect that is achievable.

Looking at Figure 2, a pump beam angle near 29.25° will allow for an angular deviation in the seed beam of almost 2.5° also centered at 29.25° . Therefore, the pump beam and the signal beam should both propagate in the same direction in order to have

the largest spread of angles in the seed beam be phase matched. Then we can see that at 0° crossing angle and 29.25° pump beam, a wavelength range of about 10nm will be phase matchable around 710nm. Therefore, using BBO we will be able to phase match the largest angular range when we using a seed at 710nm with 10nm of bandwidth, or equivalently when we are generating an idler with those same properties.

CHAPTER 2

DOUBLE-BLIND POLARIZATION GATED FREQUENCY RESOLVED OPTICAL GATING

Portions of this work originally appeared in [35] V. Chauhan, “*Pulse Compression and Dispersion Control in Ultrafast Optics*,” Georgia Institute of Technology (2010).

2.1 Introduction

Often in ultrafast-optical experiments, simultaneous characterization of two pulses is necessary. For example, in the characterization of materials, both input and output pulses must be known to measure the desired material properties[36]. Also, measuring exotic-wavelength pulses usually requires a well-characterized reference pulse at a different wavelength, thus also yielding a two-pulse-measurement problem. The same is true for very complex pulses (such as continuum), which are best measured using a previously characterized simple reference pulse[37]. As a result, a technique that can simultaneously measure two different pulses (of potentially different wavelengths) would be very useful. Each of these pump-probe type experiments would benefit from not having to make a measurement prior to conducting the experiment, as it is now necessary. A method has been proposed, in which the two unknown pulses gate each other in a nonlinear medium and the spectrally resolved signal pulse generates a FROG trace in the usual manner, called Blind FROG[38]. Blind FROG utilizes the mathematics of “blind deconvolution[22],” which is the origin of the name. Blind FROG attempts to retrieve two unknown pulses from a single FROG trace. However, for optical pulses, complete information about two unknown pulses is not available in a single FROG trace. An

additional measurement of at least one pulse spectrum is required to achieve convergence of the FROG pulse retrieval algorithm. Even with this additional spectral measurement, Blind FROG has been shown to have many nontrivial ambiguities. So, Blind FROG is not generally useful for femtosecond pulse measurement. This was pointed out by the authors in the original paper[39, 40]. Blind FROG has proven to be very useful for measuring attosecond duration pulses. However, the nonlinear interactions which give rise to attosecond pulses are much more complex than the nonlinear interactions used in FROG measurement techniques[41], and without the additional support which arises from the complex nonlinear interaction, the method has not proven useful for femtosecond pulses.

Here we show that a technique, originally proposed by Trebino, but never previously experimentally realized, which we call Double-Blind FROG, does in fact nicely solve this problem[6]. Unlike other FROG variants, in which only one FROG spectrogram is measured, in Double-Blind FROG *two* FROG traces are measured. In one trace, the first pulse gates the second pulse, and in the other trace, the second pulse gates the first. The result is the generation of two signal pulses, and hence two different traces. Generating two signal pulses is straightforward in the polarization-gating (PG) and self-diffraction versions of FROG[42-44]. Also, no modifications to the standard FROG algorithm are required. Even better, Double-Blind FROG can operate on a single-shot basis.

2.2 Single Frame Double-Blind PG FROG

This Double-Blind Polarization Gating FROG (DB PG FROG) utilizes the well-characterized single-frame geometry, which is commonly referred to as the single-shot

geometry. In this configuration, a FROG trace can be created from one single pulse out of the laser[45]. However, while our experiment utilized this geometry, our spectrometer integration time was long enough that multiple pulses entered the spectrometer during a single measurement. Changing the spectrometer integration time can change this single-frame set-up we used into true single-shot measurement.

As we discussed in Section 1.1.2.1, FROG involves making a replica of the pulse to be measured, and then scanning the pulse replicas in time relative to one another before using a spectrometer. This makes a map of delay versus frequency. The act of scanning one pulse in time relative to the other is most simply done by using a variable delay stage and making the delay stage in between pulses, but that geometry is inherently multi-shot. FROG can be performed using a single shot geometry. The single frame FROG geometry works by splitting the pulse since two replicas of the pulse are required. Then, instead of using a variable delay stage, a cylindrical lens focuses both of the beams to a line, and the two line focuses are crossed through one another at a large angle, as shown in Figure 3[46].

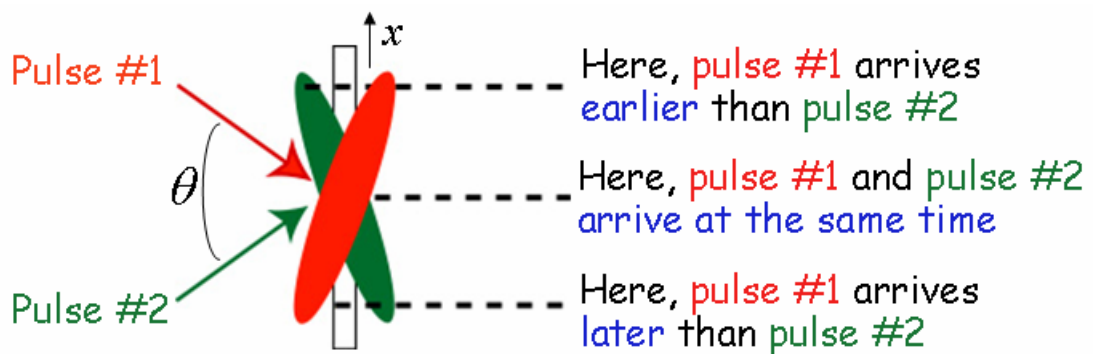


Figure 3. Single shot FROG uses transverse x position to determine delay.

At the center of the overlap region, the pulses coincide temporally. At topmost region of the crossing, the first pulse is temporally ahead of the second pulse, and at the bottommost region of the crossing, the second pulse is temporally ahead of the first pulse. The transverse position encodes the temporal delay information.

Since a FROG trace is a two dimensional object, where one image is time and the other is frequency, the single shot geometry must use a two-dimensional detector, a standard CCD camera. A lens must be used to image the transverse position on the interaction medium onto a camera so that the temporal information which is in the transverse position is recreated at the camera. The other dimension of the camera must record the spectrum, and using a grating which disperses the colors in the other dimension coupled with a cylindrical lens provides the home-build spectrometer. In the way, both the time and the frequency can be recorded simultaneously.

2.2.1 Double-Blind PG FROG Experimental Configuration

A DB PG FROG experimental setup is similar to a PG XFROG setup[47], except for the second imaging spectrometer and an additional -45° polarizer, as shown in Figure 4. In the traditional PG-XFROG set-up, the gate pulse has been previously characterized, requiring an additional measurement to be taken. The measurement part of the set-up is completely symmetric so that the interaction the first pulse experiences is identical to the interaction the second pulse experiences. The two unknown pulses gate each other in a $\chi^{(3)}$ nonlinear medium, such as fused silica. Pulse 1 is 0° -polarized and pulse 2 is 45° -polarized, with respect to the horizontal plane. A crossed polarizer is inserted into each beam path, so that no light passes through the second polarizer into the spectrometer. Both the pulses are temporally and spatially overlapped in the fused silica glass plate.

The induced change in the refractive index of the fused silica caused by the presence of pulse 1 is seen as the induced birefringence by pulse 2. Hence, pulse 1 causes time gated polarization rotation in pulse 2. By the same mechanism, pulse 2 causes a time-gated polarization rotation in pulse 1. Because the polarizations are rotated during the interaction, the generated signal passes through the crossed polarizers. Essentially, the first pulse experiences the PG FROG interaction where the second pulse acts as the gate. Simultaneously the second pulse experiences the PG FROG interaction where the first pulse is the gate. The beams are made to cross in a non-collinear manner, so that they take different optical paths after the nonlinear medium and each pulse can be isolated simply by geometrical considerations. A spectrometer is placed in each beam path, so that two FROG traces are produced, one from each interaction.

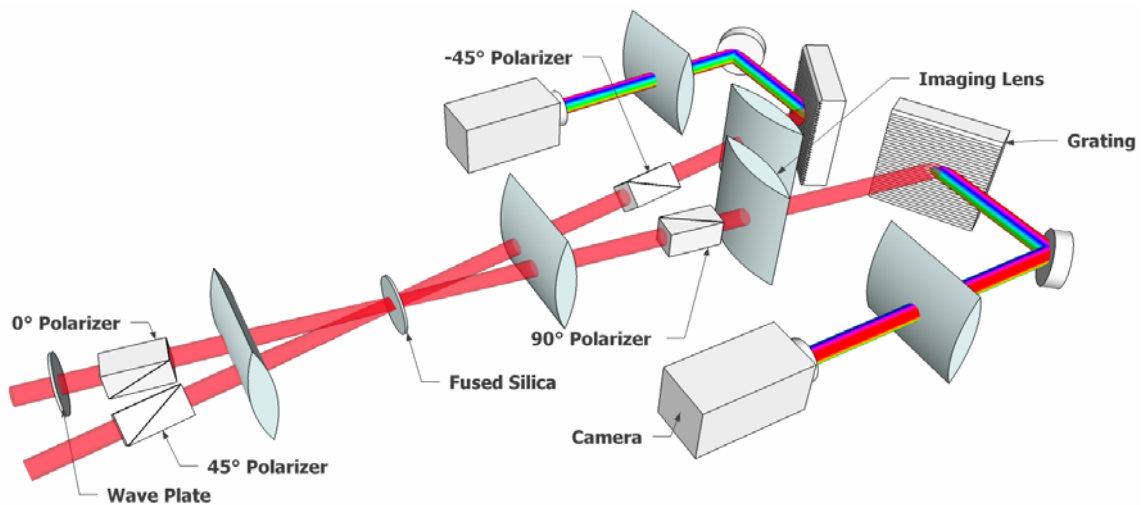


Figure 4. The schematic of a single shot double-blind PG FROG.

The double-blind technique implemented with PG FROG inherits all the advantages of PG FROG. There are no non-trivial ambiguities in PG FROG. Thus, PG FROG determines the complete and non-ambiguous pulse intensity and phase in all

known cases. A second advantage of PG FROG is that the nonlinear-optical process of polarization gating is automatically phase matched for all wavelengths and all spectral bandwidths. In the single shot FROG geometry, this allows for a large crossing angle between the beams, which in turn leads to large delay ranges. Additionally, this feature results in easy alignment as there is no strict phase matching condition to meet. Another result of this feature is that PG FROG is capable to measure pulses with extremely large bandwidths and very complex temporal waveforms. Some disadvantages result from the PG FROG geometry, too. PG FROG requires high-quality polarizers to get a high extinction ratio of at least $1:10^5$. Calcite polarizers offer the required extinction ratios but they are thick so their use results in addition of significant amounts of glass to the beam. This introduces some material dispersion and changes the pulse parameters. However, this is usually not a serious problem if the pulse being measured has a center frequency in the visible or near IR region because dispersion is relatively low at these wavelengths. Moreover, the effect of polarizers can be taken into account through post-processing at the end of the experiment and the pulse can be simply back-propagated to get the input pulse.

2.2.2 Double-Blind PG FROG Experimental Parameters

Several experimental DB PG FROG traces were generated, using a series of different pulse pairs. In each experiment, two 5mm-wide beams at a 1 KHz repetition rate centered at 800 nm from a regenerative amplifier (*Coherent Legend Elite*) are crossed at an angle of 6° in a fused silica glass plate of $250\mu\text{m}$ thickness. This crossing angle and the beam diameter correspond to a total delay range of 1.5ps. In single shot geometry, like the one being used in our experiment, there is always some temporal

broadening of the signal associated with the thickness of the nonlinear medium used, so a thinner glass plate is better. But the signal yield decreases with decreasing the thickness of the nonlinear medium, so thicker glass plates are better for this reason. We found that the use of 250 μ m fused silica plate provided a high enough signal to be measured by the spectrometer used while only resulting in temporal broadening of ~ 10 fs[6]. Figure 4 describes the schematics of Double-Blind Polarization Gating FROG (DB PG FROG) setup.

Beam 1 goes through a 0° polarizer and is focused into the glass plate to a line using a cylindrical lens of 100 mm focal length. This beam is then collimated using another identical cylindrical lens after emerging from the glass plate. Finally, it is blocked by a 90° polarizer. Similarly, beam 2 passes through a HWP to rotate polarization to 45° and then through a 45° polarizer to filter out any unpolarized light. It is then focused using the same cylindrical lens in the glass plate where it spatially overlaps with beam 1 and crosses with it in the horizontal plane at an angle of 6° . This beam, after going through the same collimating lens as beam 1, is blocked by a -45° polarizer. The polarizers used in the experiment are calcite with an extinction ratio of $1:10^5$. In the absence of temporal overlap of the pulses from the two beams, no signal can be obtained as the crossed polarizers completely block both of the signals from the cameras. We use a delay stage in one of the beam path to obtain temporal overlap between the crossing pulses. When both beams temporally coincide in the glass, a cross-correlation signal beam appears behind the crossed polarizers in both of the beam paths. For experimental convenience, we rotate the transverse spatial co-ordinates of the beams by 90° after the cross polarizers in both the beams using a periscope, thus the signal now

has the delay-axis pointing in vertical direction. Cylindrical lenses of 300 mm focal length each are used in both of the signal beams to image the delay-axis in the glass plate on to the camera. After the imaging lens, a spectrometer that uses a 600 lines/mm grating and a 100 mm cylindrical lens, spectrally resolves the cross-correlation signal, and a PG XFROG trace is obtained on each of the two cameras.

2.3 Double-Blind PG FROG Pulse Retrieval Method

Mathematically, the two traces in Double-Blind PG FROG are:

$$I_1(\omega, \tau) = \left| \int E_1(t) |E_2(t - \tau)|^2 e^{-i\omega t} dt \right|^2 \quad (2.1)$$

and

$$I_2(\omega, \tau) = \left| \int E_2(t) |E_1(t - \tau)|^2 e^{-i\omega t} dt \right|^2 \quad (2.2)$$

In the standard generalized-projections XFROG iterative phase-retrieval algorithm in which one pulse is known [4, 37, 47], the known pulse is the gate and the unknown (or the probe) pulse is retrieved. Double-Blind FROG does not have a known reference pulse available for the algorithm, but instead has two traces available from the two simultaneous measurements. The pulse retrieval step in DB PG FROG consists of a few cycles. In the first half of the cycle, the XFROG algorithm runs for a few iterations on $I_1(\omega, \tau)$ (trace 1) starting with random guesses for both $E_1(t)$ and $E_2(t)$. In this first step, the algorithm assumes $E_1(t)$ is the *unknown* and $E_2(t)$ is the known *reference* pulse. The result of this first step is not the complete pulse information, but instead is a better estimate for $E_1(t)$, which more closely satisfies the trace $I_1(\omega, \tau)$. In the next half of the cycle, this improved $E_1(t)$ is assumed to be the known pulse, and the second data set, $I_2(\omega, \tau)$, is used to obtain an improved guess for $E_2(t)$. The improved $E_1(t)$ and $E_2(t)$ thus obtained are used as the initial guesses for the next cycle. This process is repeated in our

algorithm until the resulting DB PG FROG traces match the experimentally measured trace or the minimum error is reached. Figure 5 shows the flowchart of the retrieval method.

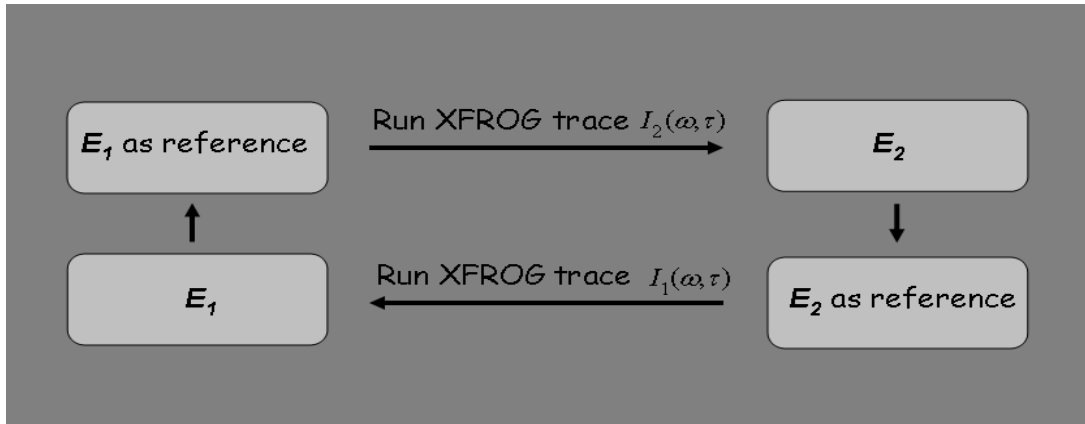


Figure 5. Each cycle during pulse retrieval in double-blind PG FROG.

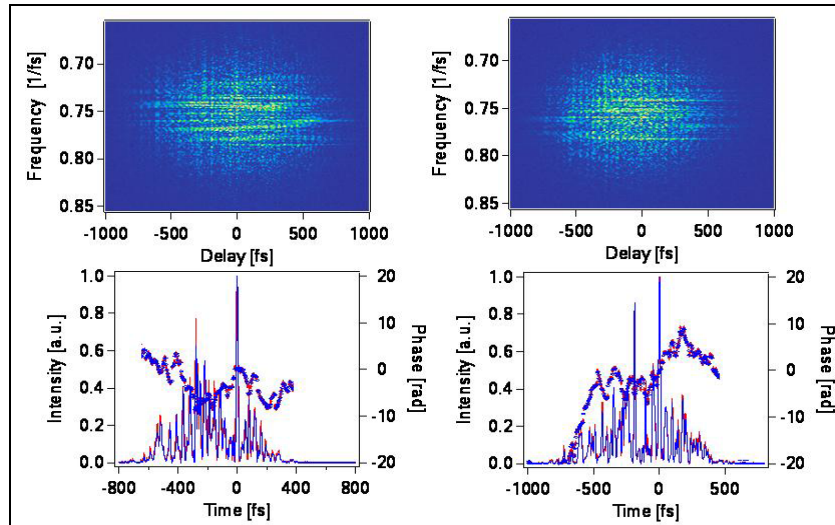


Figure 6. Simulated double-blind PG FROG traces and pulses[2].

Before running the algorithm on the traces we perform standard noise deduction steps and background subtraction. The convergence of the algorithm is defined using FROG errors, just like in other FROG techniques[6, 15]. The convergence criteria used

here is the ‘G’ error, which is the difference between the measured and the retrieved FROG traces normalized over the number of data points in the trace.

We found this process to be extremely robust. In simulations, such as Figure 6, we were able to retrieve two extremely complex pulses, with TBPs of 82 and 107, from the two PG XFROG traces generated by using them [17]. We also added 1% Poisson noise to this case to simulate experimental conditions which always involve some noise. In Figure 6, the measured and retrieved traces are shown, as well as pulses corresponding to the retrieval (bottom, blue). The pulses which were simulated to generate the traces are also shown (bottom, red) and excellent agreement is achieved. In this simulation, 1% additive noise has been added to the traces, and convergence still occurs. Note the excellent agreement, despite the complexity. So far, we have found no cases in which convergence fails to occur for Double-Blind PG FROG, even in the presence of such noise.

2.4 Experimental Results

We used PG DB FROG to experimentally measure three sets of pulses. The simpler of these pulses we verified the PG DB FROG measurements using other previously proven FROG techniques, such as GRENOUILLE. The more complex multiple pulses we generated using highly defined generation methods, such as the use of an etalon with a well known spacing, and our measurements are all in excellent agreement with our expectations. A pair of identical double pulses was also measured, but the double-blind algorithm was used to measure these identical pulses, as well as the traditional PG FROG method being run on each pulse, to demonstrate this method does

not require having two separate pulses, and that a Double-Blind FROG configuration can also be used for standard PG FROG measurements when the pulses are the same.

2.4.1 Measurement of Two Gaussian Pulses with Differing Amounts of Chirp

The first measurement we made used two pulses which were both readily measurable with GRENOUILLE, which were Gaussian chirped pulses. The two pulses have different amounts of chirp introduced to them by passing them through different lengths of glass. Pulse 1 does not travel through any additional glass and is essentially unchirped. Pulse 2 goes through an additional 4 cm of SF11 glass block which adds sufficient chirp to the pulse to significantly increase the pulse width.

The pulse width for pulse 1 was found at the Full Width at Half Maximum (FWHM) to be 104 fs. This is very close to the GRENOUILLE measured pulse width of 100 fs, shown in Figure 7. Both the DB PG FROG and the GRENOUILLE trace have an essentially flat phase across the region of interest. There is also excellent agreement between the spectrum as recovered by the DB PG FROG algorithm and the GRENOUILLE measurement. Further, FROG provides a retrieved trace, which can be compared to the measured FROG trace, and in this case there is clearly excellent agreement between the two FROG traces. Specifically, there is a G error (see section 1.1.2.1) between these pulses of 0.3 %.

Pulse 2, with a larger amount of chirp was found to be 225 fs in our experiment which is also close to GRENOUILLE measurement of 238 fs, shown in Figure 8. There is excellent agreement between the temporal phases of the two pulses. The spectra and spectral phase are also in excellent agreement, as well as the measured and retrieved FROG traces.

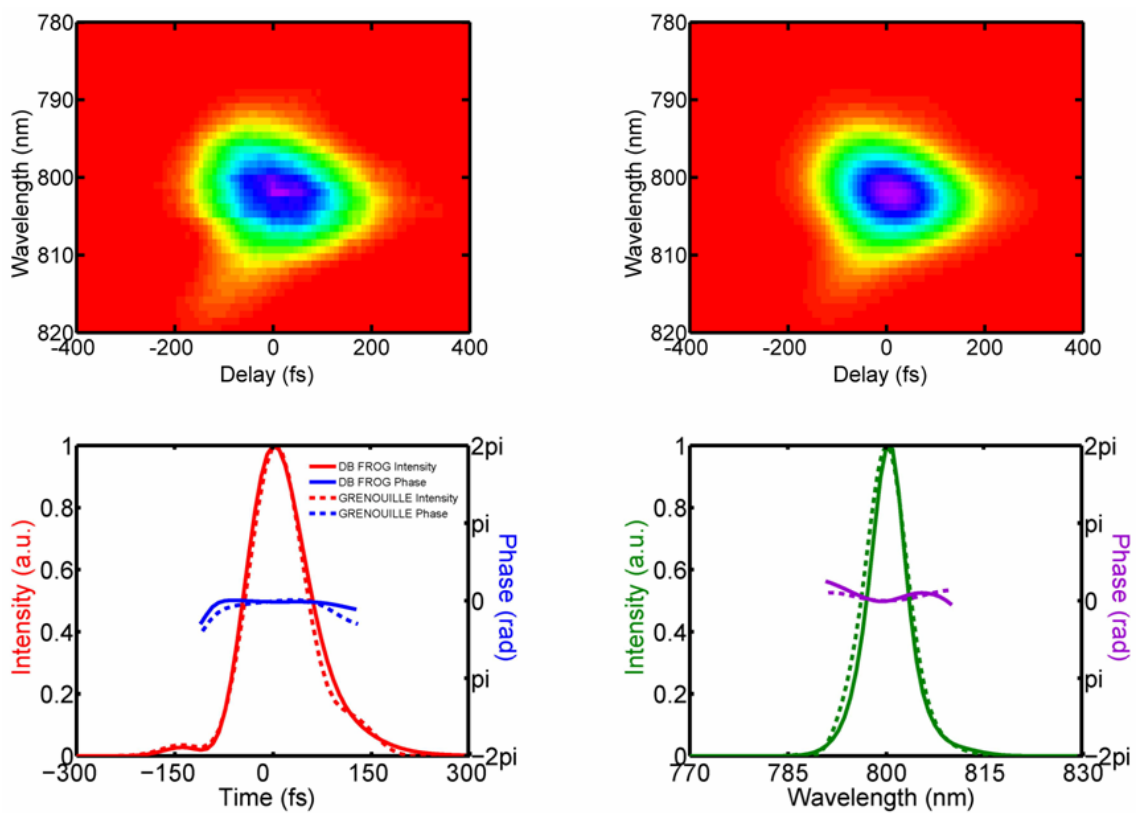


Figure 7. The first of two chirped pulses measured with DB PG FROG.

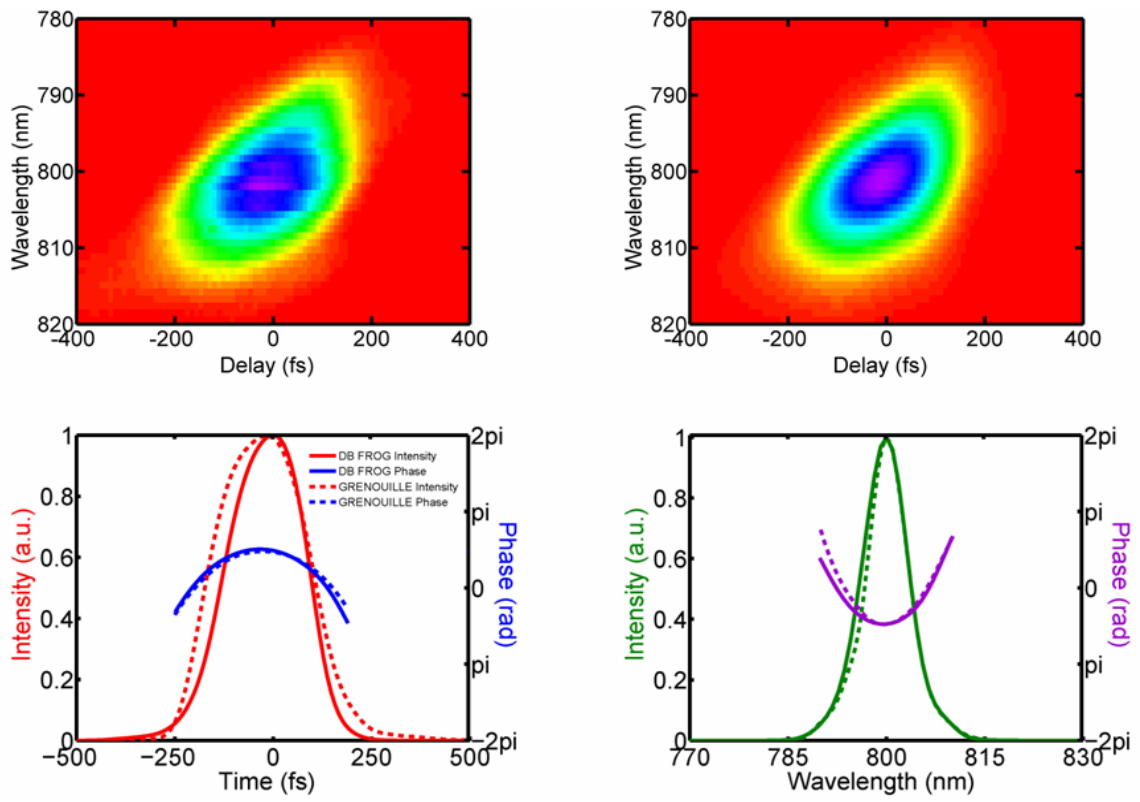


Figure 8. The second of two chirped pulses measured with DB PG FROG.

2.4.2 Measurement of a Gaussian and a Pulse Train from an Etalon

To measure a more complicated set of pulses, where the pulses were significantly different, we measured a pulse train from an etalon and a simple pulse. We placed an etalon[48] with the spacing of 23.5 microns in one of the beams in DB PG FROG to produce a pulse train. An etalon is an optical cavity with a partially reflecting back mirror, so that as the pulse travel back and forth through the etalon some of the energy escapes from the cavity on each trip. The etalon which we used has essentially zero energy left in the optical cavity after three passes off the partially reflecting surface.

The second pulse which we used for the DB PG FROG measurement was a simple Gaussian, similar to the unchirped pulse in the chirped pulse measurement. Thus, we obtained two traces: one in which the pulse train was gated by the simple pulse (Figure 9) and the other in which the simple pulse was gated by the pulse train (Figure 10). The etalon spacing corresponds to peak locations at 0 fs, 156 fs and at 312 fs, and the spectral peak separation of 13.5 nm. The etalon had an air gap, so light travel at the speed of light in air through in the empty region between the mirrors. The etalon spacing of 23.5 microns results in light moving between the mirrors in 78.3 fs, so the peak separation we expect is 156.6 fs between the first two peaks and 313 fs between the first and third pulse, which is in excellent agreement with the values we recovered from DB PG FROG. The Gaussian pulse was measured by DB PG FROG to be 85 fs long, in excellent agreement with the GRENOUILLE measurement result of this pulse of 83 fs which is demonstrated in Figure 10.

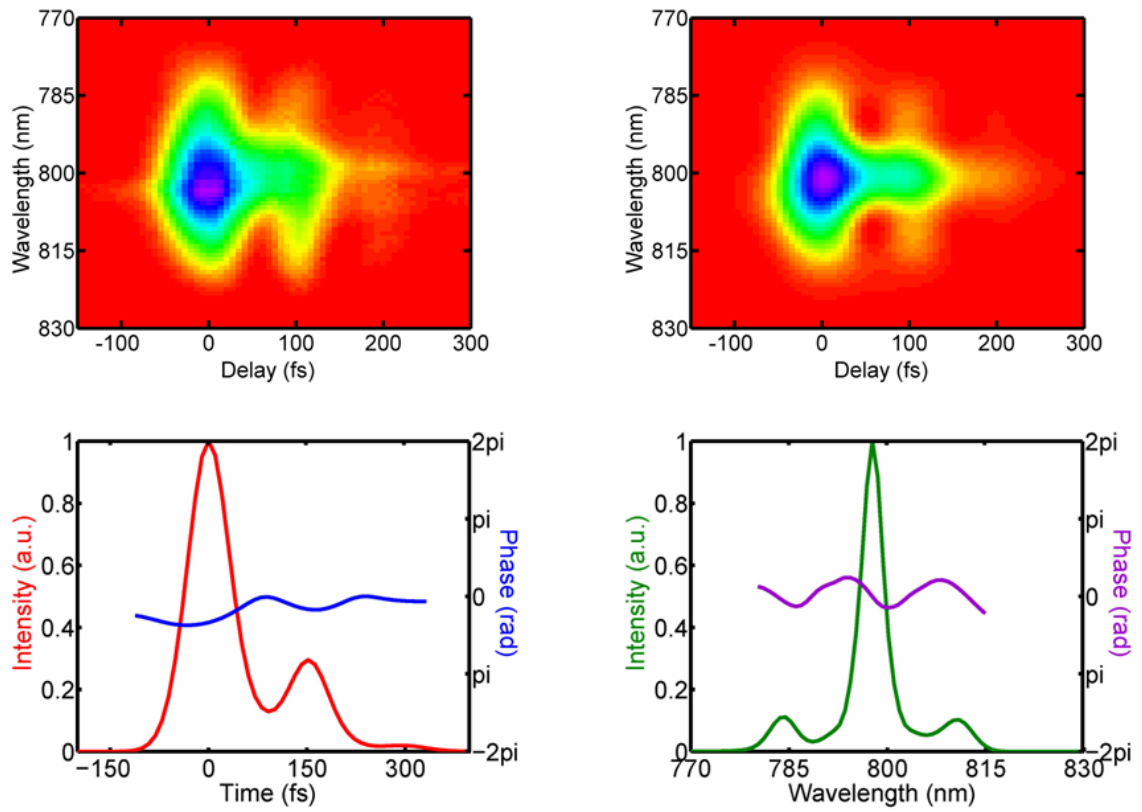


Figure 9. A pulse from an etalon measured with DB PG FROG.

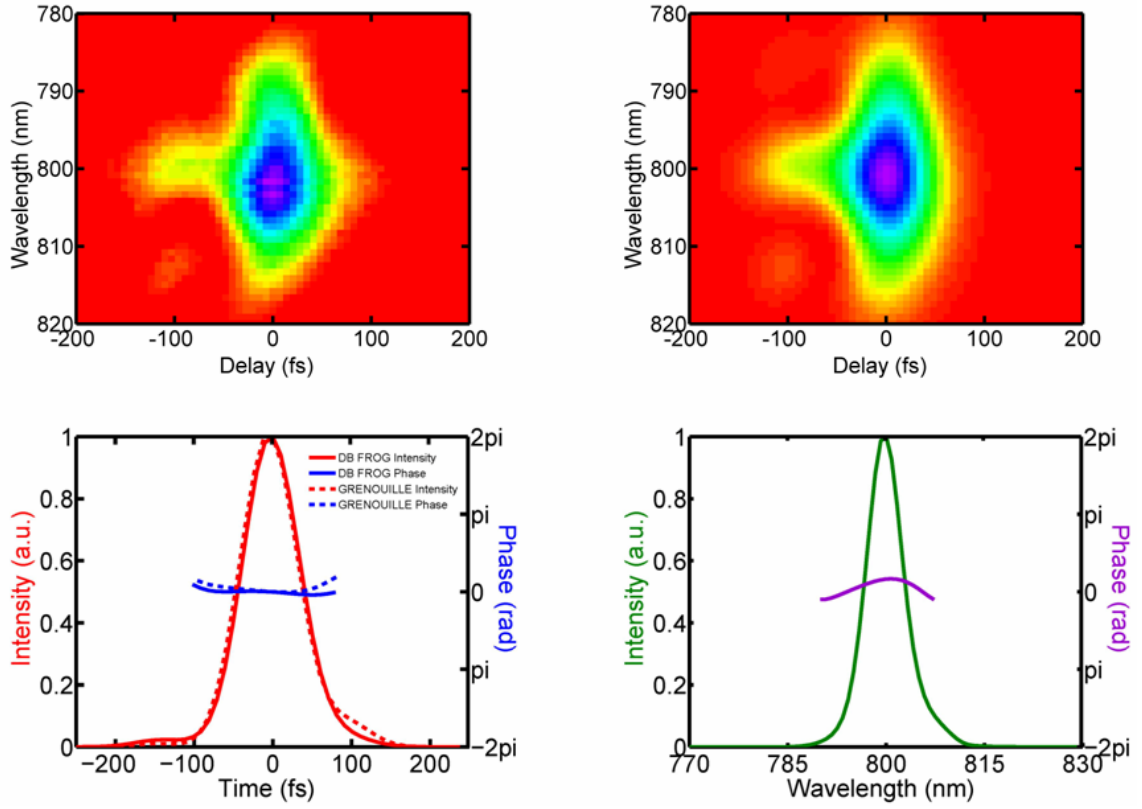


Figure 10. A simple pulse used to measure the etalon pulse with DB PG FROG.

2.4.3 Measurement of a Two Double Pulses

We measured a pair of identical double pulses to demonstrate that once the DB PG FROG technique has been experimentally set up, many other variants of FROG are also accessible, including standard PG FROG as well as PG XFROG, making the experimental apparatus extremely versatile. Using the DB PG FROG algorithm, we were able to retrieve both pulses when they were identical as well as when they were different (see Figure 11 and Figure 12).

The separation between the peaks was 526 fs in double pulse 1 and 518 fs in double pulse 2. Using an ocean optics spectrometer the temporal separation was found to be 516 fs. We retrieved these pulses using both the PG FROG algorithm as well as the DB PG FROG algorithm. In both cases, as we expect, the discrepancies between the two measurements lies well within the error margins due to calibration errors.

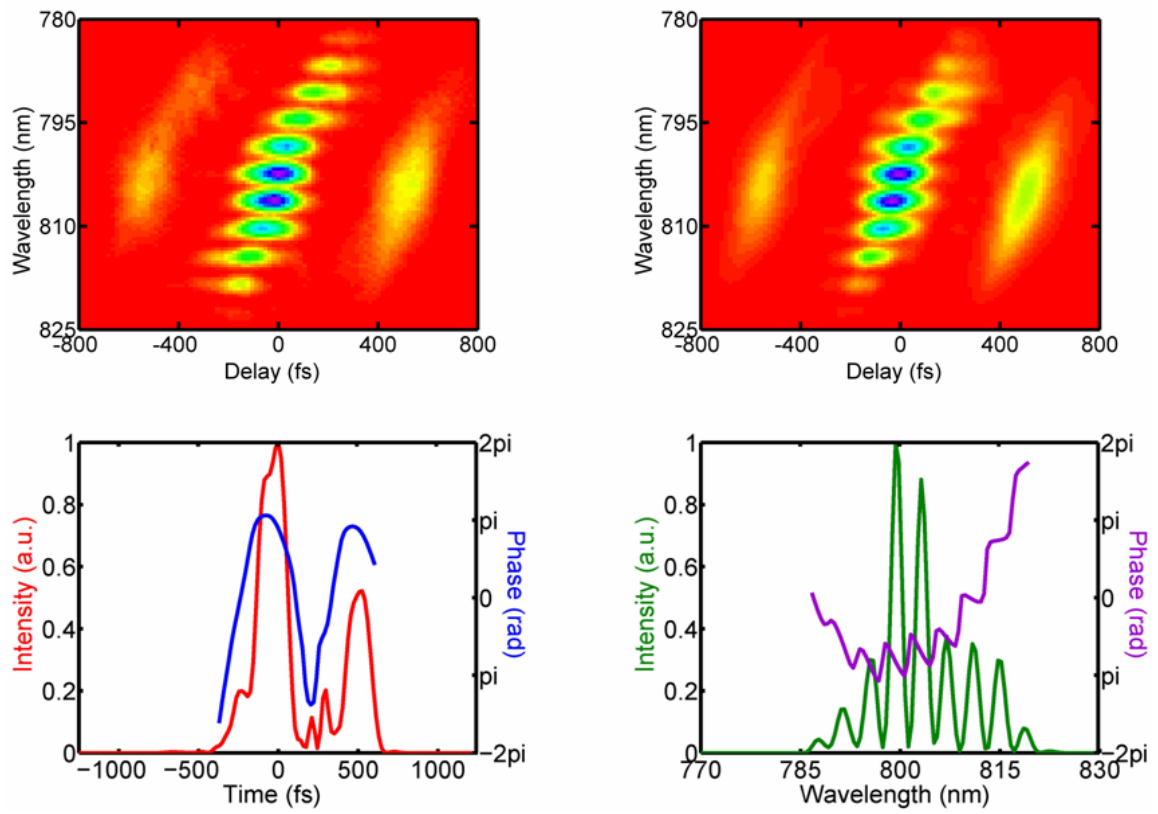


Figure 11. The first of two identical double pulses measured with DB PG FROG.

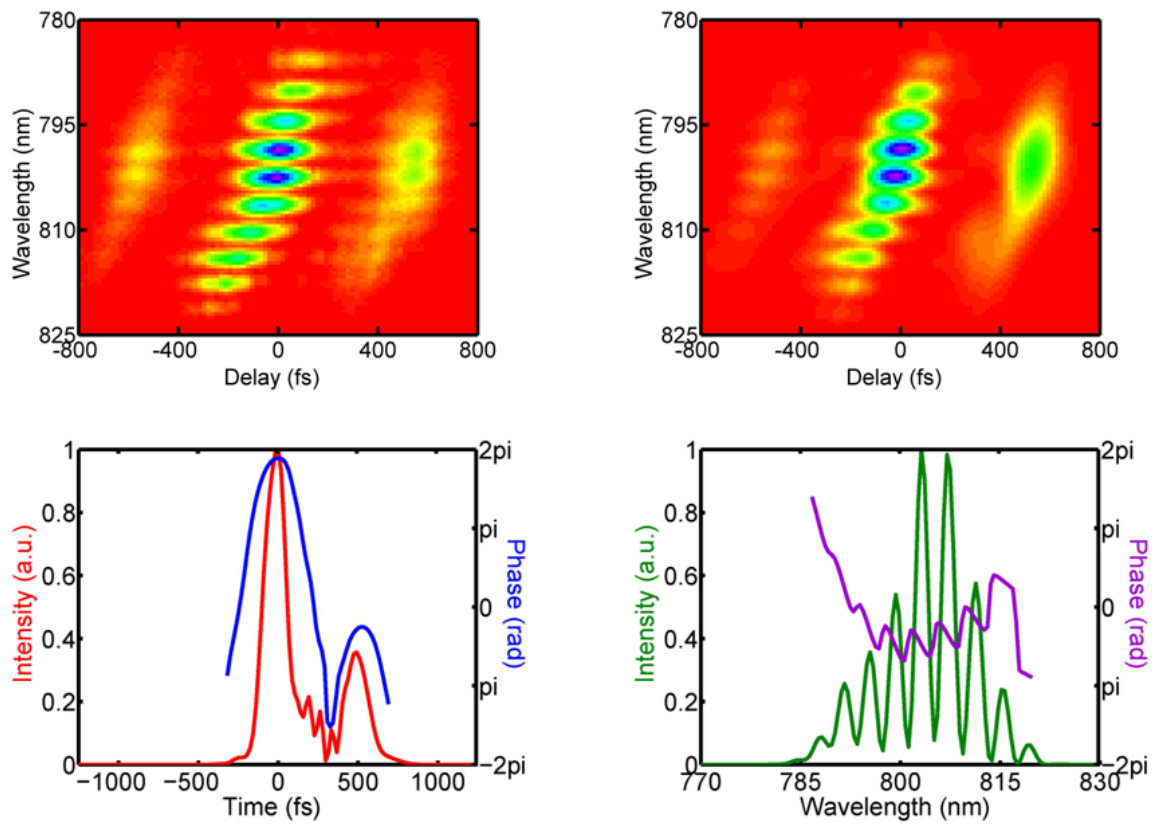


Figure 12. The second of two double pulses measured with DB PG FROG.

2.5 Conclusion

We have demonstrated a single-shot method for measuring two unknown pulses using one device, Double-Blind PG FROG, which has no non-trivial ambiguities, has a reliable algorithm, and is automatically phase matched for all spectral bandwidths. We have measured identical pulses as well as extremely disparate pulses with this technique and have shown it to be robust for pulse measurement. We have measured pulses of comparable temporal duration and pulses whose duration are significant different, and have found no trouble in making any of these measurements. This method should find use in numerous applications. In simulations, this method has proven to be extremely robust, measuring very complicated pulses with TBPs of ~ 100 even in the presence of noise. In the future work, we will try to measure more complicated pulses, even continuum, using this method.

CHAPTER 3

THE HISTORY OF NONLINEAR OPTICS FOR IMAGING

3.1 Introduction to Nonlinear Optical Imaging

Nonlinear optics has several desirable properties which can be applied to image bearing signals. Nonlinear imaging involves imaging an object (or target) and mixing it nonlinearly with another wave. These techniques can result in amplification, wavelength conversion, spatial-filtering in either the real space or the Fourier domain, time-gating and phase conjugation. Many of these techniques can be applied simultaneously to the initial target. An imaging system images or focuses the target onto a nonlinear medium, where an intense beam mixes with it and the nonlinear processes are generated.

3.2 Optical Parametric Amplification Imaging

The process of OPA allows for wavelength conversion. This will allow for infrared signal to be detected on conventional CCD detectors. While many interesting signals are in the infrared, detection of these wavelengths significantly lags behind detection of visible wavelength.

3.2.1 The First Demonstration of OPA Imaging

The first demonstration of applying nonlinear optical techniques to imaging was in 1968[49]. In that demonstration, a seed beam was generated using a Xenon lamp and the pump beam was a narrowband ruby laser centered at 694.3nm. The Xenon lamp beam was in the mid-infrared location was scanned through a variable density plate, which consisted of bars with different widths. A measurement was made at 1000nm, and as the infrared beam was scanned the bars were recreated point by point. The gain in this

configuration was estimated to be 10^{-7} because phase matching was not idealized and very narrow line width beams were used.

3.2.2 Previous OPA Imaging of 4 lp/mm

Another study using OPA for imaging by Lantz and Devaux[50]. Lantz and Devaux used picosecond pulses to pump, so they again had narrow line widths. As a result, they were only able to achieve at most a gain of ~ 30 , and were only able to amplify or convert the wavelength of 4 line pairs per millimeter (lp/mm) because they were required to use a 5mm thick nonlinear optical medium. In some of their experiments[51], they used a 400nm pump beam and an 800nm seed beam, generating an 800nm idler beam. They were able to use a type-II configuration so that the polarization of the generated beam made it separable from the input beam. In other experiments, they used an infrared seed with a 400nm pump beam, generating a visible idler wavelength[52]. Because of the use of a thick crystal and a temporally long pump beam, they were limited in spatial resolution (see section 4.5) and these studies were limited to a maximum space-bandwidth product (see section 5.3) below 5600.

3.2.3 OPA Imaging and Spatial Filtering

OPA imaging has been applied to both monochromatic[53] and polychromatic[52] images have been amplified. When OPA is performed to amplify or frequency-shift an image, the interaction takes place between the input beams in the nonlinear medium, but different interaction planes can be used, depending on the imaging system used. The OPA crystal can be placed at an image plane, which is then re-imaged onto the detector[52, 54]. Spatial frequency filtering in the real image domain is possible, but requires changing the crystal angle, which changes the spatial frequency

transfer function of the system[51]. Placing the interaction plane at a focus causes the interaction to be in the Fourier plane of the image[15]. Using this interaction geometry should allow much greater control of the spatial frequency transfer function [55, 56] by spatially shaping the pump beam.

3.2.4 OPA Imaging Without Lenses

Another unique property of OPA imaging, which may potentially prove useful, is that the difference-frequency generation (DFG) beam is the phase conjugate of the input image beam, and, with OPA, the phase conjugation occurs in the forward direction. As a result, OPA imaging can be performed without the use of imaging lenses[57-60]; if the same wavelength is used for the OPA and the DFG beams (that is, operating at degeneracy), an exact replica of the spatial distribution of the input, but with gain, appears the same distance after the nonlinear medium as the object before it.

3.3 Sum Frequency Generation Imaging

Both the DFG and the SFG processes can be used to convert the wavelength of an image from the infrared into the visible, and so both nonlinear methods have been applied to image bearing signals. When SFG is used, there is no exponential gain of the target. However, because this gain does not occur, SFG does not require having the pump beam as the highest frequency in the interaction; many more wavelengths can be accessed in this interaction.

3.3.1 Sum Frequency Generation of a Complex Image

There has been success in wavelength-converted images using Sum Frequency Generation (SFG) applied to complex images. To determine the complexity of an image,

we utilize the two dimensional space-bandwidth product (SBP)[61] (see section 5.3). The most complex image wavelength-converted using SFG in the real-image plane had a SBP of $\sim 16,000$ [62]. Using SFG with the Fourier plane as the interaction plane, results of a SBP greater than 63,000 have been obtained[63]. These SBPs are significantly better than has been reported previously utilizing OPA as the nonlinear interaction. With the crystal at the image plane, the best previously reported complexity contained 4 line-pairs/millimeter (lp/mm) in both the horizontal and vertical directions, and achieved amplification by an average factor of ~ 30 , and had an SBP of $\sim 6,000$ [52]. The greatest gain in an image to which OPA has been applied using the Fourier interaction plane yielded a gain of $>10^3$ [55], but with a resolution of only 1.25 lp/mm, and a SBP of only ~ 15 . Further, only the DFG beam could be recovered; the OPA beam was below the detector threshold.

3.4 Other Nonlinear Optical Processes for Imaging

3.4.1 CARS imaging

One process which has been used to experiment with amplified imaging is Coherent Anti-Stokes Raman Amplification (CARS). Here, a pump beam excites a medium so that the medium becomes the gain medium. The signal is then introduced into the excited medium. The signal is amplified and the idler results to conserve momentum. There are two major drawbacks to this method however. First, the medium in which CARS is performed is usually cell of gas which must be maintained at a particular temperature and pressure, neither of which are concerns when using a non-linear crystal as the interaction medium. Second, CARS is not a parametric process. A parametric process is assumed to occur instantly with the arrival of the pulses. In CARS,

however, the pump pulse must prime the medium, and this is not an instantaneous process. The delay in such a system must be optimized not for temporal overlap, but for best amplification. The greatest amplification can occur hundreds of picoseconds after the pump pulse arrival. This limits the potential repetition rate of such a system to the excitement and relaxation time of the medium instead of to the repetition rate of the laser systems involved. Moreover, if there is any fluctuation in the temperature or the pressure of the gas, which can be expected to happen upon repeated use of the gain medium, the ideal timing between the pump laser and the seed image will fluctuate in a random fashion.

3.4.2 Four Wave Mixing Imaging

Another potential candidate as a non-linear process is four wave difference frequency generation. In OPA, a single pump photon at the highest frequency is split into a signal and idler photon. With four wave mixing, two pump beams at a central frequency could be utilized. Then these two pump photons can both be destroyed to create the signal and idler frequency. The advantage over OPA imaging is that the idler can have a frequency lower than the pump beam, so that the fundamental frequency from a Ti:Sapphire laser can create a visible idler instead of a near-IR idler. The problem with using four wave mixing is that there are undesirable interactions which will occur simultaneously with the desired process. Specifically, the two pump beams existing at the same time in the same location and being the same color will interfere, generating a transient optical grating. This grating will interact with the seed beam, causing diffraction and distorting the input image. If this can be overcome or limited, four wave mixing could be a viable process for frequency shifted imaging.

CHAPTER 4

THEORETICAL CONSIDERATIONS FOR OPTICAL PARAMETRIC AMPLIFICATION IMAGING OF COMPLEX IMAGE-BEARING SIGNALS

Portions of this work appear in [64] P. Vaughan and R. Trebino, “*Optical-parametric-amplification imaging of complex objects*,” *Opt. Express* 19, 8920-8929 (2011).

4.1 Introduction to OPA for Complex Imaging

The ultrahigh intensities available from ultrafast-laser technology allow access to a wide range of high-intensity phenomena and techniques. Whereas earlier laser systems required tightly focused beam spots in order to achieve sufficient intensities, recent advances in Ti:Sapphire regenerative amplifiers (“regens”) allow high-intensity interactions of unfocused beams with relatively large diameters. Vastly improved stability in such amplifier systems also makes practical previously impractical highly nonlinear processes.

4.1.1 Laser Stability and OPA Imaging

Optical parametric amplification (OPA)[65], in particular, which experiences gain that is an exponential of the pump-beam intensity, benefits greatly from these technological advances. OPA has long been used to nonlinear-optically amplify weak input signals[66], as well as to wavelength-convert them, usually from the infrared into the visible[67]. Unfortunately, due to its highly nonlinear nature, OPA is very sensitive to and severely limited by shot-to-shot jitter of the pump laser. Pulses that are too weak

can yield no signal, and pulses that are too intense can yield outputs that saturate the detectors or, worse, damage the crystal. Such issues significantly complicate applications of OPA, and, as a result, OPA, perhaps more than any other optical process, benefits from the high intensity and, especially, the vastly improved shot-to-shot jitter of these laser systems.

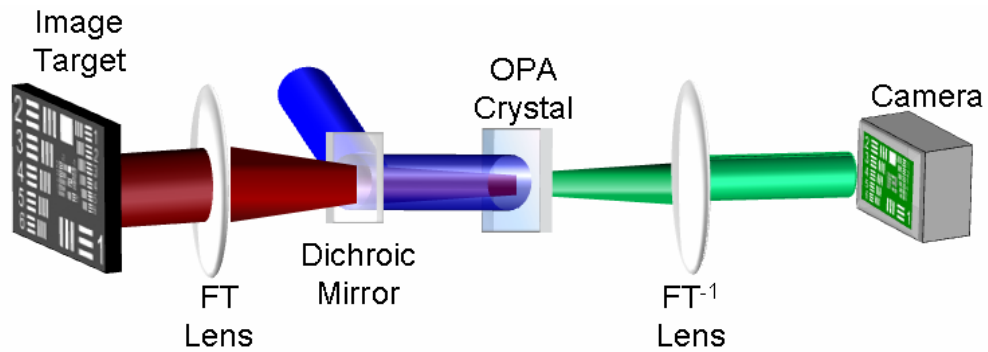


Figure 13. A typical Fourier transform OPA imaging apparatus.

The use of OPA for imaging applications, shown in Figure 13, should benefit greatly. In such a system, an image target is illuminated with infrared light and transferred by a lens to a nonlinear crystal. A shorter-wavelength pump beam (shown in blue) overlaps the image-bearing signal at the nonlinear medium. The OPA process generates an intense replica of the image at a new (typically visible) wavelength. It simultaneously amplifies the infrared light (the amplified IR beam is not shown). The imaging or inverse Fourier-transforming (FT^{-1}) lens then images or inverse Fourier transforms the field for detection at the camera.

4.1.2 Goals of OPA Imaging Studies

The goal of such studies is the application of OPA for amplifying and wavelength-shifting a complex (i.e., interesting) image – one bearing a large spread of spatial frequencies in both the horizontal and vertical dimensions. One major advantage to using OPA is the ability to achieve high gain. The highest gain ever reported using OPA imaging was in a ballistic-imaging experiment, where a gain of 10^4 was demonstrated[68], although this gain was across a one-dimensional image in which the detector position was scanned and the detected intensity mapped over many pulses.

4.1.3 Scope of This Work in Comparison to Previous Works

Here we extend this technology to the imaging of a more complex object and report two-dimensional OPA Fourier-plane imaging of spatial features from 1.1 to 10.1 line pairs/millimeter (lp/mm) in the vertical dimension and from 2.0 to 16.0 lp/mm in the horizontal dimension. We observe a gain of ~ 100 , and, although our images were averaged over many shots, we used a single-shot geometry, capable of true single-shot OPA imaging. To our knowledge, this is the first Fourier-plane OPA imaging of more than a single spatial-frequency component of an image. The two-dimensional SBP for our Fourier-plane OPA imaging system was $\sim 46,000$ and the two-dimensional SBP for the DFG image was $\sim 30,000$.

4.2 Optimizing gain in OPA imaging

There are two main limitations on the achievable gain and image fidelity in OPA imaging. Both involve phase matching, whose condition for the beams of interest must be satisfied:

$$\omega_{PUMP} - \omega_{OPA} = \omega_{DFG} \quad (4.1)$$

$$\vec{k}_{PUMP} - \vec{k}_{OPA} = \vec{k}_{DFG} \quad (4.2)$$

where ‘PUMP’ refers to the pump (the shortest wavelength and most intense) beam, ‘OPA’ to the amplified beam at the input wavelength, which in our case is the infrared 930nm input, and ‘DFG’ to the wavelength-converted beam, which in our case was the visible 700nm beam.

4.2.1 Phase matching Types

As is well-known for all nonlinear-optical processes, achieving phase matching across the entire pulse spectral bandwidth limits the crystal thickness and hence the gain efficiency[69]. The phase matching process can be performed in several polarization configurations referred to as type-I and type-II phase matching. In these configurations, the phase matching angle will depend on the polarization on the interacting beams. Here, we have used type-I phase matching, where the pump beam is extraordinarily polarized, so that the OPA and DFG beams are both ordinarily polarized.

4.2.2 Limitations on Phase matching Efficiency

The phase matching process is not only limited by efficiency and spectral bandwidth consideration, but has a limited geometrical acceptance angle (see section 4.6)[70]. Since the wave vectors in (4.2) are vectors, their lengths depend on the wavelengths, their directions depend on input angles of the interacting beams. In many OPA experiments, the change in the phase mismatch (the difference between the left hand and right hand sides of equation (4.2)) as the wavelength is changed is minimized. This configuration is commonly referred to as non-collinear OPA, and can lead to amplification across a broad spectral range[71]. For imaging applications, it is more

important to limit the change in phase mismatch as the angle of the interacting waves is changed[4].

The second limiting factor in an OPA imaging system is OPG[72, 73], which involves phase matching of beams not of interest. It is the generation of parametric super-fluorescence from noise background light due to the use of an input pump of high intensity. The background, also referred to as Optical Parametric Generation (OPG), degrades the amplified image and competes for available pump-beam energy. For uniaxial crystals, OPG is generated as a pair of concentric rings, each of longer wavelength than the pump, and the longer wavelength ring has a larger diameter. As a crystal's phase matching angle is changed, the diameters and central wavelengths of the OPG rings change, so that the phase matching condition continues to be satisfied for the central wavelengths of each ring.

4.3 OPTICAL PARAMETRIC GENERATION

OPA occurs when the seed beam that is supplied is amplified. However, it is possible that with a sufficiently intense pump beam, no supplied seed beam is necessary. This is referred to as Optical Parametric Generation or Parametric (Super)fluorescence. This arises when there is zero input in either the signal or the idler. This cannot be predicted from the coupled wave equations as the process is entirely quantum mechanical in nature while the wave equation is classical[74].

4.3.1 Parametric Amplification of Noise

Once a single photon has been generated through this quantum mechanical zero-point energy amplification, this photon acts as a seed beam to continue the amplification process and a significant signal can be build up[75]. Since this arises not from a supplied

signal but from nothing, OPG acts as a noise background to the OPA process. However, the OPG threshold is higher than the threshold to stimulate OPA, and if the pump beam is of the appropriate intensity to pump OPA but not to generate OPG, this may be avoided.

There are further potential complications which can arise from OPG beyond it acting as background. OPG will appear with the most intensity along the direction where $\Delta\vec{k}$ is minimum. This is where phase matching is greatest, and from the coupled wave equations, this is also the direction where the gain will be greatest. Optical Parametric Generation requires only the input of a pump wave, and in a uniaxial crystal, phase matching will occur in a cone which is symmetrical about the pump beam and whose apex angle satisfies the vector phase matching equation for the frequency generated.

The projection of these cones onto a camera will result in rings of diameters which depend on the frequency, as shown in Figure 14. When attempting to get high gain from an OPA Imaging system, there is a limitation on the pump power which can be used because of the OPG background that will be generated if the pump intensity is too high. The gain factor is exponential with the power of the pump beam, so having a pump beam which is just below the OPG threshold will result in the greatest amplification without introduction of a background.

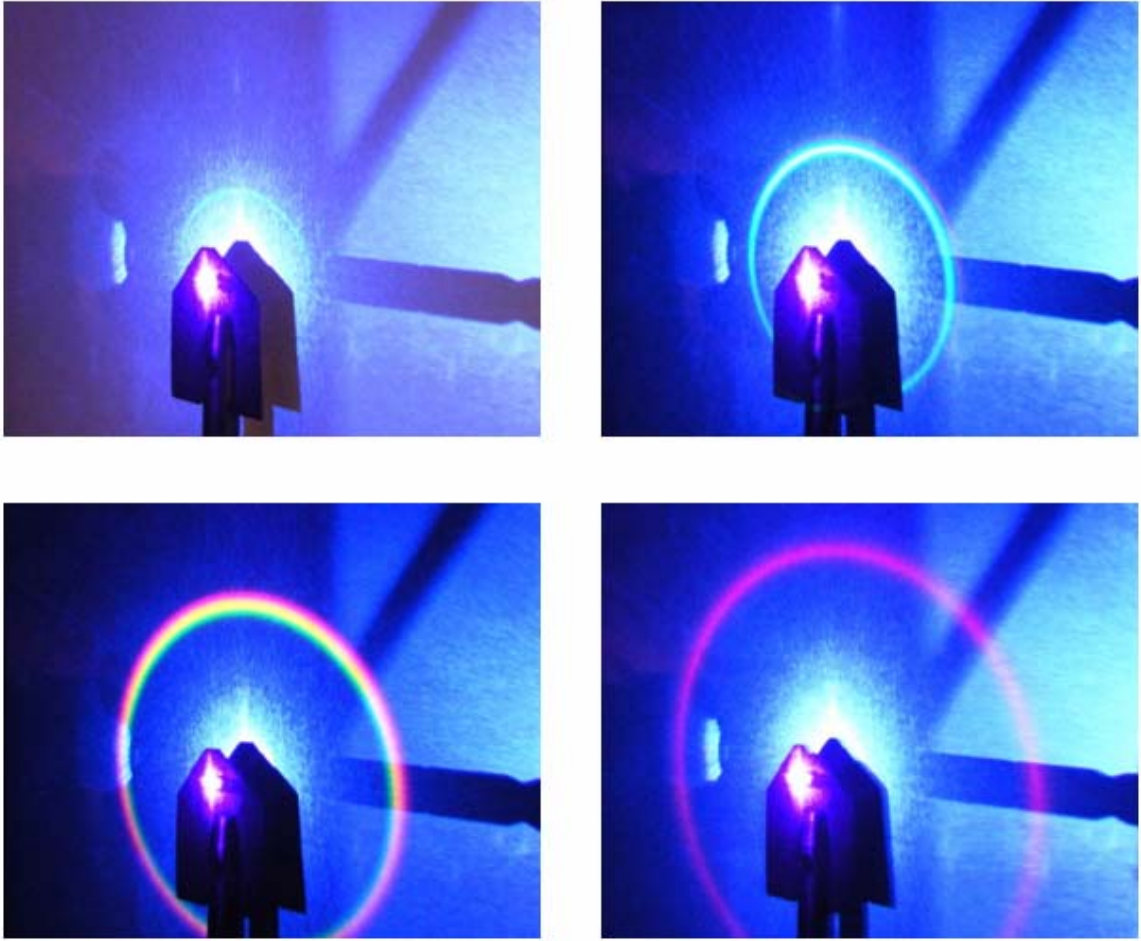


Figure 14. OPG rings at several different crystal angles.

4.3.2 OPA in the Presence of OPG

When the gain in the signal is greater than the background generated, it might be argued that the signal-to-noise ratio can be improved even while the background is being generated. There is a second issue which arises when OPG occurs along the same direction as the signal. The OPG and the signal can be thought of as two temporally overlapping beams with the same spectral content, and these two beams will interfere with one another.

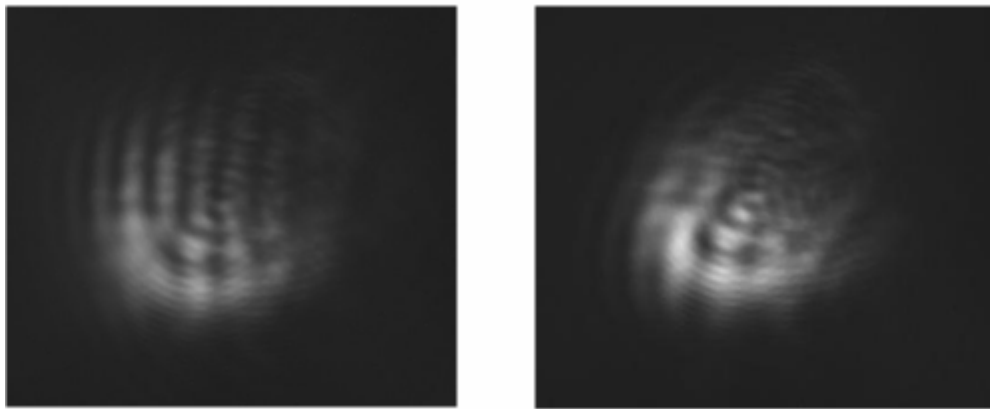


Figure 15. OPA and OPG interfere when both processes occur simultaneously.

In Figure 15 there is a demonstration of this, where an Airy disk pattern signal is overlapped with an OPG ring. The stripes which occur happen because of the interference between these two beams. This demonstration occurred in a non-collinear geometry, and the stripes were tilted by slightly altering the crossing angle. This interference between the OPG ring and the seed image will cause severe and unremovable distortions when applying this to imaging.

4.3.3 Gain Limitations Due to the Presence of OPG

While the direction in which OPG occurs is also the direction in which the gain will be highest, it is not the only direction where phase matching is possible because there is a bandwidth to the processing of phase matching (described in section 1.2.3.1), amplification can occur in a direction other than the OPG direction. When the frequency to be phase matched does not correspond to the frequency at which OPG is generated best, high amplification can occur in one direction while OPG occurs in a different direction.

To minimize the problems presented by OPG, we chose crystal parameters so that the smaller OPG ring occurred at an angle outside the area of the image and used an aperture to separate the OPA image from the OPG background. We utilized a completely collinear beam geometry for the pump, OPA, and DFG beams, yielding less gain because the OPA process was not perfectly phase matched. Nevertheless, we were still able to achieve over two orders of magnitude of amplification across the pulse spectrum. We also observed similar gain across a wide range of spatial features (that is, angles). We also used wavelength filters to separate the beams after the OPA crystal to isolate the OPA or DFG beam.

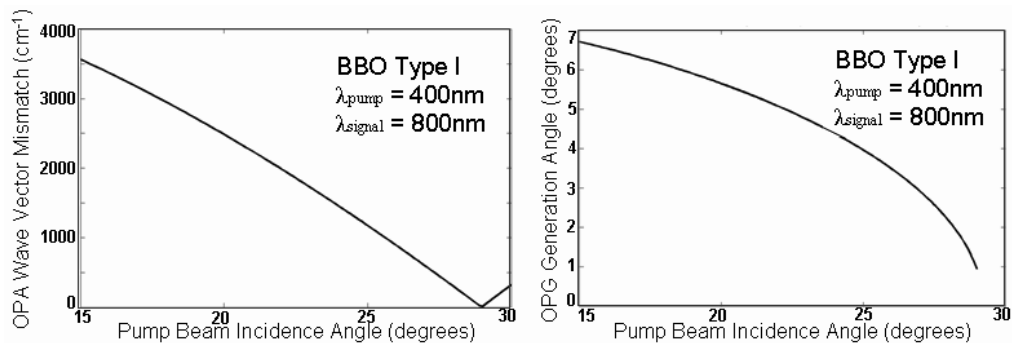


Figure 16. Wave-vector mismatch for and the OPG-ring angles.

Specifically, for sufficient separation of the OPA and OPG in our experimental parameters, the OPG ring had to make a minimum angle of $\sim 2^\circ$ relative to the pump direction. If we were using an 800nm seed beam, perfect phase matching would have occurred with a crystal angle of 29° , but, at this angle, the smallest OPG ring would have occurred at 0.95° . In order for the OPG ring to occur at an angle of 2° so that it would lie well outside the image, the crystal had to be used at an angle of 28.2° , as seen in Figure 16. Had we been able to use the crystal at the ideal phase matching angle of 29° , the mismatch would only be $< 10 \text{ cm}^{-1}$, and the OPA gain would have been much larger, but the resulting OPA wave-vector mismatch was $\sim 300 \text{ cm}^{-1}$. Fortunately, since we are interested in using a seed beam at 930nm, the wave vector mismatch is further improved by using this frequency.

4.4 Spectral Considerations for OPA Imaging

We measured the spectrum of the input beam and the amplified output beams. We found that, despite the phase-mismatch, the only noticeable spectral effect is a slight increase in bandwidth, shown in Figure 17, which is an expected effect during OPA when either of the input beams is not well-collimated[71].

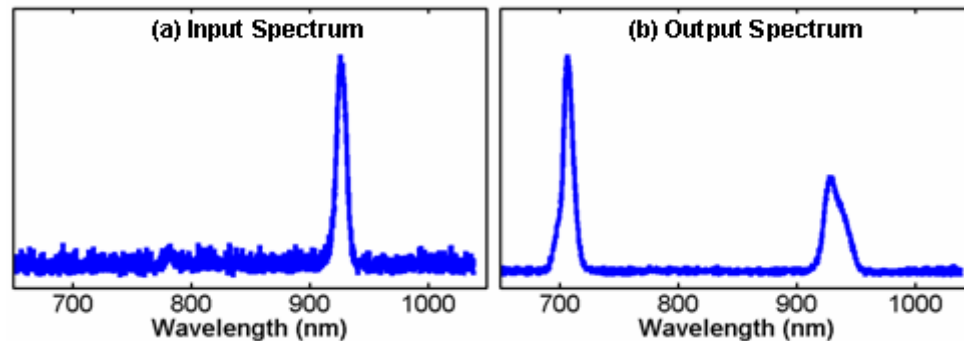


Figure 17. The input spectrum and the two output spectra after the OPA.

The 930nm peak is the only input, used as the seed beam. The output spectrum (Figure 17) is clearly broadened from the input spectrum. This result occurs during OPA when either of the input beams is not well-collimated. In OPA imaging, an image bearing signal cannot, by definition, be well-collimated. This broadening of the spectrum for the input wavelength will always occur. The output beam at the difference frequency is also clearly seen to have less bandwidth than the output OPA beam. This is also expected, as conservation of energy dictates that the bandwidth of the lower wavelength output beam during OPA will be narrower than the bandwidth of the longer wavelength beam. The spectrum is also distorted from the Gaussian input. There is a distinct shift in the spectrum with higher intensities occurring at the lower signal wavelength in Figure 17. This occurs because the gain in the process is a function of the wavelength, and changes by a non-negligible amount across the 10nm of seed beam bandwidth.

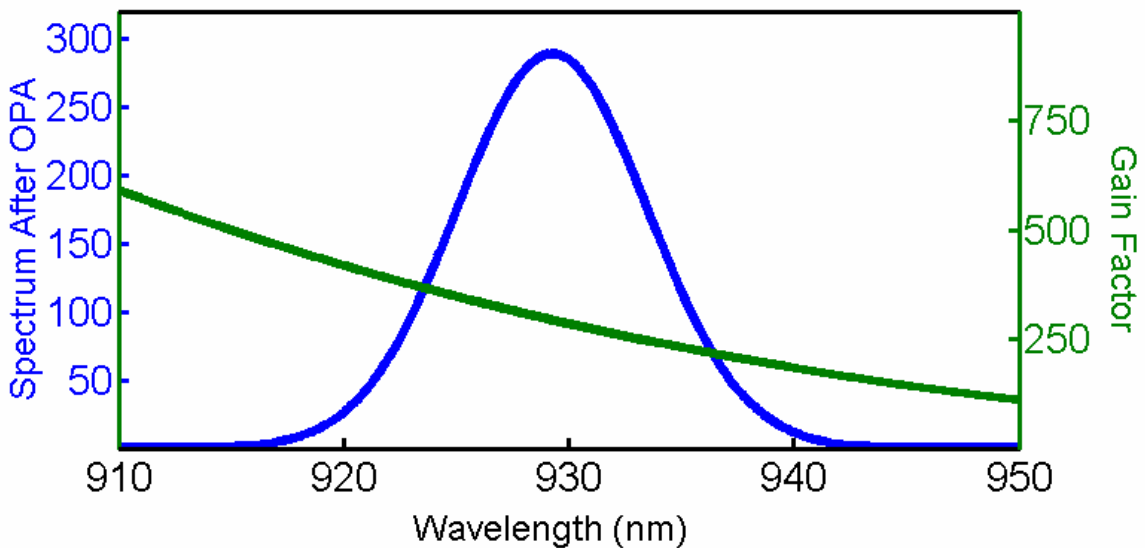


Figure 18. The gain changes over the seed pulse bandwidth.

The gain factor in the presence of phase-mismatch was calculated to change by ~30% over the bandwidth of the pulse spectrum (Figure 18). This slightly higher gain at lower wavelengths results in this spectrum which is slightly shifted towards lower wavelengths from the input seed spectrum. This shift is by less than 1nm the 930nm center wavelength for our 10nm FWHM seed pulse.

4.5 Maximizing spatial resolution in OPA imaging

In addition to the above gain limitations, there are geometrical factors that limit the spatial resolution of OPA imaging systems. These include geometrical smearing due to the thickness of the nonlinear medium[6], spatial imperfections of the pump beam, which are imprinted onto the amplified and wavelength-converted beams, and the angular acceptance of the nonlinear medium. In this section we explain how we maximized the spatial resolution of our imaging system by minimizing the geometrical distortions due to each of these effects.

4.5.1 Geometrical Smearing

The problem of geometrical smearing arises during amplification of the real image plane when the output beam and the input image-bearing beam cross at an angle (see Figure 19). This leads to an amplified point generated at the leading edge of the crystal which differs in transverse position from amplified points generated later in the crystal. The amplified beam interacting with the image-bearing beam at different transverse positions in the crystal results in a single image point mapping to a range of transverse points in the resulting image, that is, an out-of-focus image.

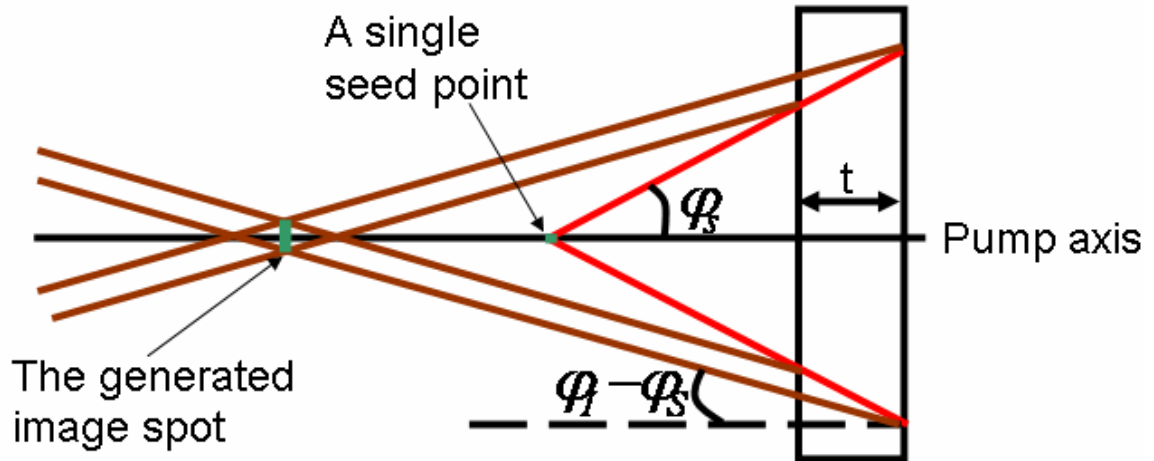


Figure 19. Geometrical smearing arises due to crystal thickness.

In a real-image plane geometry, the way to limit geometrical smearing is to use an all-collinear beam geometry[76]. When the input and output beams are perfectly collinear, the transverse positions of the OPA beam do not vary across the crystal length, and geometrical smearing does not occur. However, while this holds perfectly for interactions of two plane waves, the definition of a complex and interesting image is a beam that contains a nonzero range of wave vectors. By its nature, then, an image cannot be perfectly collimated. Propagating the beams in a non-collinear geometry would have introduced larger geometrical smearing effects, but even use of a collinear geometry cannot completely eliminate geometrical smearing from OPA imaging.

In the Fourier plane geometry, however, the image points are essentially located at the nonlinear medium since the Fourier plane and the nonlinear medium coincide. Using the Fourier plane as the plane of interaction will naturally limit geometrical smearing, as long as the Fourier plane is present at every point throughout the thickness of the nonlinear medium [76]. In this geometry, the effect of the crystal thickness is naturally minimized.

4.5.2 Pump Beam Divergence

The pump and seed beam, and how the overlap and cross in the crystal, will further limit the resolution and the efficiency out of the image amplifier system. In section 4.5.1, we discussed how the crystal thickness affects the resolution. Here, we discuss the influence of the pump beam divergence and how to overcome this. The effect of the pump beam divergence is shown in Figure 20. The divergence of the pump beam is shown to further increase the size of the output spot in Figure 19 by an amount β .

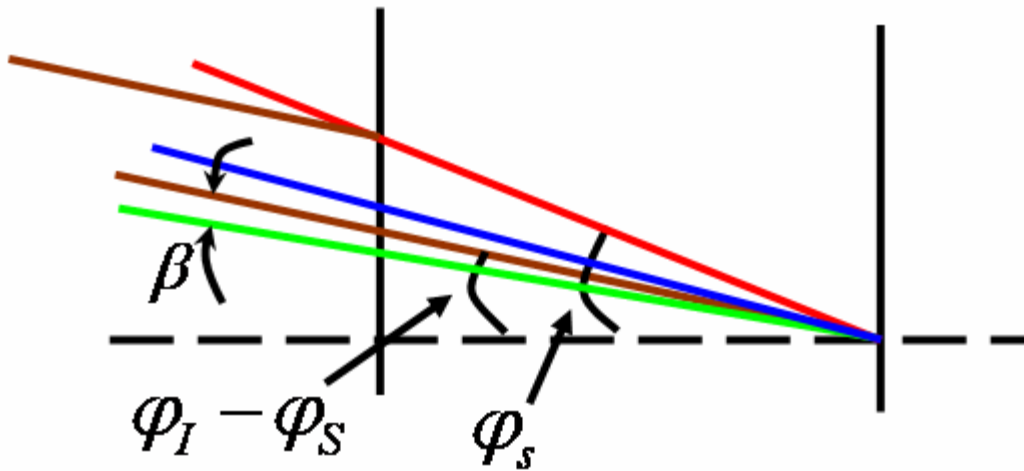


Figure 20. A diverging pump beam increases the point spread function.

A spatial filter is designed to minimize the pump beam divergence (see section 5.1.1), and the lens system which de-magnifies the pump following the spatial filter needs to further ensure that this divergence is minimized. The lens system can be used to collimate the beam so that its divergence is at a minimum when it reaches the nonlinear medium.

Utilizing a high-intensity amplified femtosecond pump pulse, we were able to use a much thinner nonlinear medium (1mm thick) than previous efforts. Previous demonstrations, conducted using picosecond pump pulses[52], required nonlinear media

cm in length, or required multiple passes through the crystal[55]. Both of these configurations used a real-image plane geometry, with the result of significant geometrical smearing.

4.5.3 Effect of Pump Beam Spatial Profile

Another geometrical issue arises from consideration of the quality of the pump beam used. The highest resolution requires using a spatially smooth, collimated beam as a pump[76]. In previous demonstrations of OPA imaging, and in most other applications of OPA, the pump beam was focused in order to achieve the high pump intensities that OPAs require. Utilizing our high-power regen, we were able to spatially filter (section 5.1.1) our beam to produce a clean spatial mode and pump our OPA with a well-collimated, unfocused, pump beam while still achieving peak intensities of over $1\text{GW}/\text{cm}^2$. This was done with a pump beam of 2mm diameter.

A second benefit of using a large-diameter pump beam is that it allows for overlap between a greater portion of the image-bearing beam with the pump beam. The interaction region between the pump beam and the image-bearing beam in the nonlinear medium acts as an aperture for the output from the OPA imaging system. When the interaction plane is the Fourier plane, the pump-beam size acts as a Fourier filter (see section 6.2.1), removing the highest spatial frequencies (and hence the detail) from the image. When the interaction plane is the image plane, the pump beam acts as an aperture applied directly to the image, and it limits the size of the image.

4.6 Angular Acceptance in OPA Imaging

A final consideration which must be taken into account in OPA imaging systems is the angular acceptance of the OPA imaging system[77]. By their nature, images

contain a spread of spatial frequencies, and therefore propagate in a range of angles. If the phase matching of the OPA system changes significantly over a range of input angles for the seed beam, an image will not be produced at the output. The maximum spatial frequency that any OPA imaging system will be able to accept is therefore limited by phase matching considerations. Moreover, a somewhat uniform amplification across the entire image is desired in most OPA imaging applications. The gain profile, which is determined by the phase matching, needs to be constant over the angular range of the image. It is customary in OPA imaging to define a boundary for OPA imaging acceptance angles as the angular range over which the gain is always at least 50% of the maximum gain for ideal phase matching[77].

For 1mm BBO in a type-I configuration, the half angular acceptance in the two transverse dimensions of $\Delta\phi = \sim 17$ milliradians for the difference-frequency wavelength of 700nm. The crystal has a half-angular acceptance at the 930nm OPA signal wavelength of $\Delta\phi = \sim 23$ milliradians (see Figure 21).

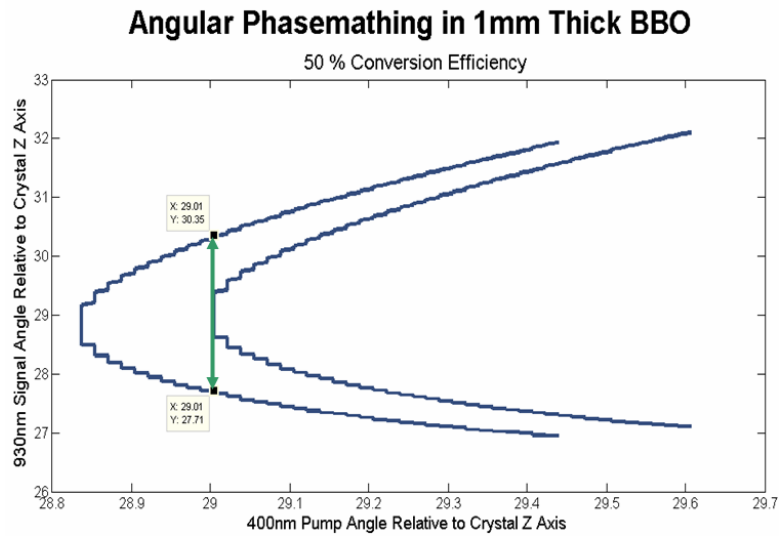


Figure 21. Angular phase matching at 50% conversion efficiency.

To determine the angular acceptance, the pump beam angle and the seed beam angle are plotted against one another (similar to section 1.2.3.1.2), but instead of determining the perfect phase matching angle, we consider only the 50% conversion efficiency angles, as we defined 50% conversion efficiency as phase matched. These angular ranges correspond to an expected maximum resolution of $\sim 30 \text{ mm}^{-1}$ for both the OPA beam and DFG beam wavelengths.

CHAPTER 5

EXPERIMENTAL DEMONSTRATIONS OF OPTICAL PARAMETRIC AMPLIFICATION IMAGING OF COMPLEX IMAGE-BEARING SIGNALS

Portions of this work appear in [64] P. Vaughan and R. Trebino, “*Optical-parametric-amplification imaging of complex objects*,” *Opt. Express* 19, 8920-8929 (2011).

5.1 Experimental apparatus for OPA imaging in the Fourier plane

In our experimental OPA imaging apparatus (Figure 25), we amplified the output from a KM Labs kit oscillator with a Coherent Legend Elite Regenerative Amplifier to produce 40fs pulses centered at 800nm with pulse energies of 3mJ at a repetition rate of 1kHz. We performed second-harmonic generation in a 1mm BBO crystal to produce a beam at 400nm with 1mJ per pulse, which was used as the pump in the OPA process.

5.1.1 Vacuum Spatial Filter

While the beam from the regen was fairly unstructured to begin with, we built a spatial filter to remove the small amount of structure present in it. It used a 50 μ m wire die as the spatial-filter pinhole. The pinhole was contained in a 4Torr vacuum chamber to avoid nonlinear breakdown in air.

Any spread in the wave-vector content of the pump beam will lead to a decrease in the resolution from an OPA Imaging system (see section 4.2.2). In order to remove any non-forward-propagating wave-vectors, a spatial filter may be used. A spatial filter is a device where which consists of a lens system and a pinhole. The first lens focuses

the beam. At the focus of this lens is the Fourier Transform of the input beam a distance f before the lens (see Appendix A). The pinhole is placed at the focal plane of the lens and is constructed so that it has a diameter corresponding to the focused spot size of the desired input beam. Thus, any Fourier component which was not desired in the input beam is blocked by the pinhole. A second lens performs the inverse Fourier Transform to recover the desired spot. This system results in the desired spatial profile, but with a loss of energy corresponding to any of the blocked wave-vectors. How this system should perform is shown in Figure 22. Essentially, such a filter only allows through the Gaussian TEM₀₀ mode.

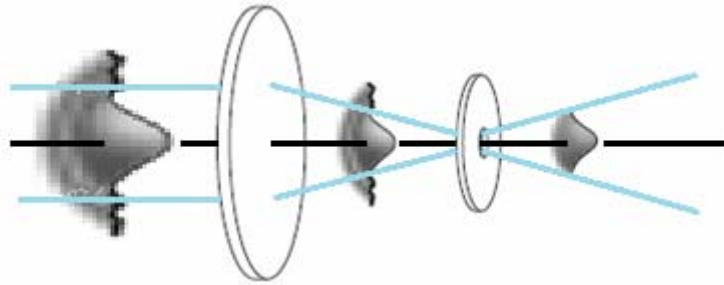


Figure 22. A spatial profile cleaning pinhole system.

With the Coherent Legend 3mJ/pulse system, a modification of this system is required. The pump beam used in these experiments is the second harmonic of the fundamental. Second harmonic generation in the system is at 45%, resulting in 1.3 mJ/pulse of 400nm pump energy. When an ultrafast pulse with this much energy is focused in air, there is a nonlinear breakdown of the air, and supercontinuum is generated by the N₂ in the air (see section 1.2.2.4). This supercontinuum generation ruins the spatial profile of the beam, which completely defeats the purpose of having a spatial filter. In order to avoid the generation of supercontinuum, the pinhole must be placed

under vacuum. A vacuum spatial filter is a vacuum chamber with transmitting windows on each end and a pinhole contained in the middle. In constructing a vacuum spatial filter, the windows must be sufficiently far from the pinhole that supercontinuum is not generated in the windows. As the beam focuses through the pinhole, its power is decreased, and the distance between the pinhole and the exit window can be shorter than the distance between the input window and the pinhole.

To align such a filter, the simplest method is to decrease the pump beam intensity in a fashion that does not alter the beam path, to remove the input window and align the pinhole in air, then compensate for the input window deflection of the beam. Aligning a beam into a micrometer diameter pinhole enclosed in stainless steel tubing without being able to see the pinhole is extremely difficult. The effect of a spatial profile filter can be quite dramatic when the initial beam carries a large amount of distortion, as demonstrated in Figure 23.

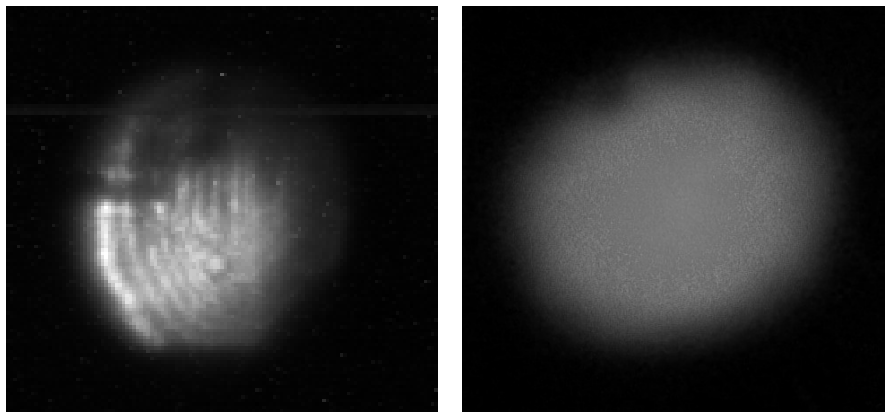


Figure 23. A very poor spatial profiles is spatially filtered.

When this level of filtering occurs, the decrease in beam power can be greater than 90%, as a very poor spatial mode will contain little of the energy in the TEM_{00}

mode. Therefore, we took care to have our initial input beam be as spatially uniform as possible so that our output beam would be as energetic as possible. While the mode from the regen itself is very clean, we used the second harmonic as the pump beam.

Unfortunately all nonlinear processes greatly magnify any spatial imperfection into the mode to being with. However, since OPA requires the highest frequency wave to be the pump, we were forced to perform SHG to get the pump beam if we wanted to convert an IR image into the visible range.

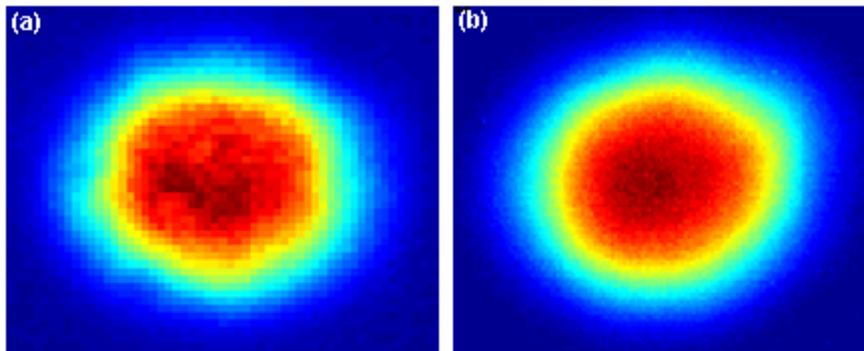


Figure 24. Profiles of the pump beam both (a) before and (b) after filtering.

The output from our vacuum spatial filter was 0.6mJ per pulse, so the decrease in energy was only $\sim 50\%$ from the unfiltered profile. This filtered beam was down-collimated utilizing a positive and negative focal length lens pair so that the pump beam was collimated with a diameter of 2mm. The result of this spatial filter was to smooth the intensity profile, as shown in Figure 24. Even when the pump beam has significantly less distortion than shown before the filter, the spatial profile before filtering always displays several hot spots in the most intense regions of the beam. These hot spots are smoothed out by the filter. If these hot spots had been present in the beam, there would have been non-uniform amplification across the input image during the OPA process.

The shot-to-shot pulse-energy jitter from the Coherent Legend Elite at the fundamental frequency was 0.56%. The shot-to-shot pulse-energy jitter at the second harmonic, which was used as the pump beam in our OPA after passing through the spatial filter was 0.94%. This clean spatial profile and stable shot-to-shot intensity allowed us to pump our OPA with a stable laser source.

5.1.2 Description of the Entire Apparatus

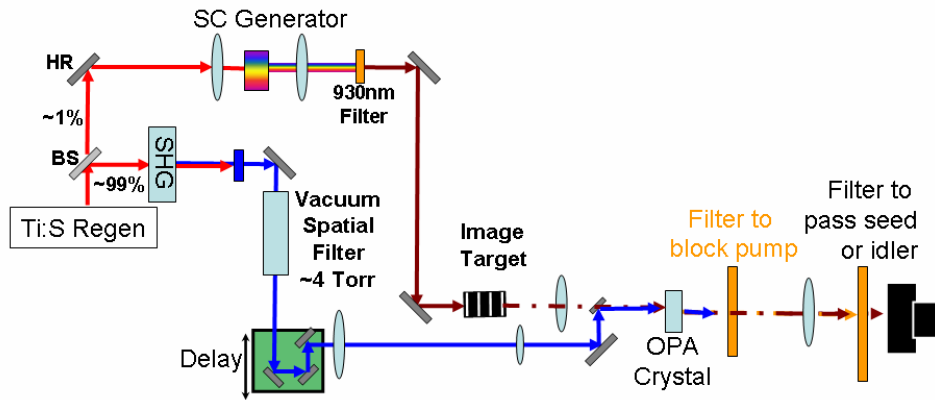


Figure 25. OPA imaging experimental apparatus.

The device, shown in the schematic of Figure 25, works as follows. The output from the amplifier was split into two beams. Most of the light was frequency-doubled to act as the OPA pump. The rest generated supercontinuum by focusing a small fraction of the 800nm pulse through 3mm of fused silica. This continuum was then passed through an infrared band-pass filter, which transmitted 10nm of bandwidth centered at 930nm. This infrared wavelength range was selected for two reasons. First, the DFG beam through this process was centered at 710nm which is the wavelength range we determined to be most desirous in section 1.2.3.1.2. Also, this allows for demonstrating a

shift from the infrared into the visible. Second, this infrared wavelength is detectable by the PixeLink PL-A741 CCD array we used to record the OPA beam, allowing measurement of the amplification of the infrared beam—a desirable situation in many practical applications of OPA imaging.

The image was generated by placing a transmitting USAF 1951 target (see Appendix B) in the infrared beam path. The output face of this target was placed one focal length before a 150mm-focal-length lens. At the focal plane, a 1mm-thick type-I BBO crystal, cut at a phase matching angle of 29° , acted as the OPA medium. The 400nm pump beam was e-polarized, and interacted with an o-polarized seed beam. The generated OPA beam and DFG beam were both o-polarized as a result of this Type-I interaction. This crystal was mounted on a rotation stage so that it could be angle-tuned. Because the nonlinear medium was placed at the focus of this lens, the Fourier plane of the image became the interaction plane for the OPA imaging system. To perform the inverse Fourier transform on the amplified OPA image or on wavelength-converted DFG beam, an achromatic 100mm second lens was placed its focal length after the nonlinear medium. The ratio of the focal lengths of these two lenses resulted in a de-magnified image at the camera.

5.2 Experimental Results and discussion

Our illuminated target, weak input image, OPA amplified image, and DFG wavelength-shifted image are shown in Figure 26.

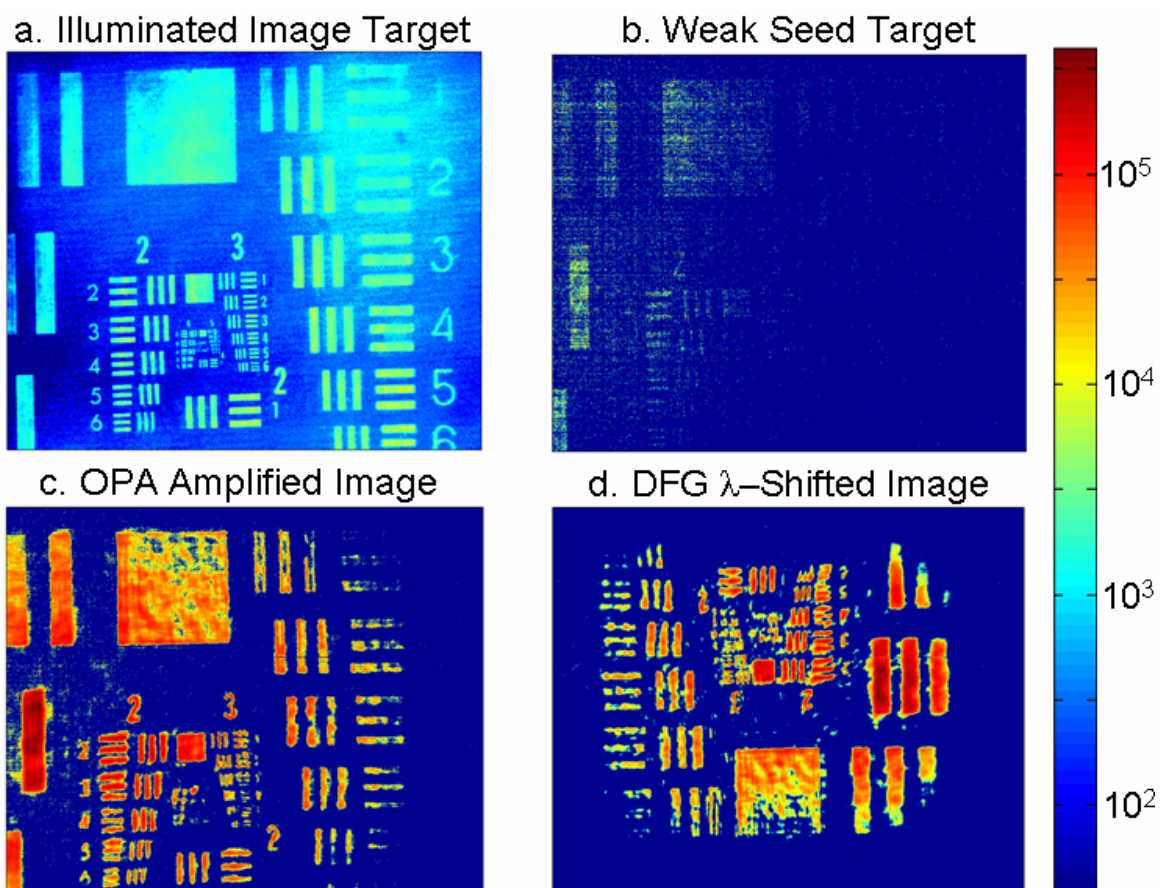


Figure 26. Results of image amplification and image wavelength shifting.

This demonstration focused on achieving an amplification of two orders of magnitude. We demonstrate both amplification of an IR image and simultaneous amplification and wavelength down-conversion of a single image, both of the USAF 1951 test pattern. Both this amplification and the wavelength conversion occur simultaneously, so a band-pass filters at the appropriate wavelength must be used to isolate either the OPA beam or the DFG beam.

Figure 26(a) is the USAF 1951 image target, containing resolvable spatial frequencies from 1.1 lp/mm in the vertical direction and 2 lp/mm in the horizontal direction to 57 lp/mm in both directions. Before performing amplification, we reduced the supercontinuum intensity, as seen in Figure 26(b). With the supercontinuum intensity lowered so that the 930nm input image was close to the camera noise floor, we were able to measure the amount of amplification which occurred across the image. The non-uniform spatial profile of the supercontinuum results in most, but not all, of the image being below the noise floor of the detector.

We consider first the OPA image at 930nm (Figure 26(c)). To measure the amount of gain in the amplified infrared image, we deliberately decreased the supercontinuum beam intensity in order to generate a weak infrared seed (Figure 26(b)). This decreased the input intensity to a level comparable with the noise floor of our camera. After the OPA crystal, the OPA amplified image (Figure 26(c)) increased to an intensity just below the saturation level of the detector, implying an OPA image gain of ~ 100 (the camera had only 8 bits of dynamic range). While features as fine as 57 lp/mm were resolvable in the input image, the Fourier plane OPA interaction acts as a low-pass filter for spatial frequencies in the image due to the resolution limitations discussed in

Section 3. In our image, observable features spanned the range from 1.1 to 10.1 line pairs/millimeter (lp/mm) in the vertical dimension and span from 2.0 to 16.0 lp/mm in the horizontal dimension.

Figure 26(d) shows the DFG wavelength-converted image from the 930nm infrared input wavelength to a 700nm visible wavelength. The DFG image had resolvable features spanning the range from 1.1 to 10.1 lp/mm in both dimensions. This is a slight decrease in resolution compared with the amplified OPA image, which is due in part to the fact that this image has somewhat more noise than the amplified OPA beam. The wavelength down-converted (frequency-upconverted) image is rotated 180° with respect to the input image and OPA image. This occurs because the OPA image and DFG image are phase-conjugates of one another. Thus, the lens which acts as an Inverse Fourier Transforming lens applied to the OPA image acts instead as a Fourier Transforming lens on the DFG image. There is also angular demagnification that occurs during the conversion process[76], and so we observe a reduced image size. This angular demagnification occurs in all images where wavelength conversion shifts an image from a longer wavelength to a shorter one, and the amount of demagnification is the ratio of the input to output wavelength, which here will be a demagnification of $930/700 = 1.3$, which is the demagnification that we observe.

5.3 The Space-Bandwidth Product (SBP)

The SBP[61] is a dimensionless measurement that nicely quantifies the complexity of the measured image. One way to construct this quantity is to take the product of the spatial extent of an image and the resolution (measured in spatial

frequency) of that image. For a two-dimensional image, a SBP is computed for each transverse dimension, and the total SBP is the product of these two SBPs.

5.3.1 SBP of Our Measurement and Comparison to Previous Work

For the wavelength-unshifted OPA image, in the vertical dimension, we resolved in the amplified image features with a spatial resolution as fine as 10.1 lp/mm. The spatial extent of vertical features in our image spanned from the top edge of the group-0 features to the bottom edge of the group-2 features. This was a distance of ~ 8 mm. The amplified image had a vertical SBP of ~ 150 . In the horizontal dimension, the features spanned ~ 9 mm with resolution of 16 lp/mm, so the horizontal SBP was ~ 300 . The amplified image therefore had a two-dimensional SBP of $\sim 45,000$.

A similar calculation shows that, because of the slightly lower resolution achieved in the wavelength-shifted DFG image, the two-dimensional SBP for the wavelength-shifted image was $\sim 30,000$.

The largest two-dimensional SBP previously reported for OPA imaging in which the Fourier plane was the plane of interaction[55] we calculated to be ~ 15 . The best previous measurement for OPA imaging using a real image plane as the plane of interaction[52] achieved a SBP of $\sim 6,000$.

5.3.2 Limitations on the Measurement of the SBP

Recording the space-bandwidth product requires measuring the spatial extent of the recovered image as well as the ability to resolve the finest features of the image. It is often the case, as it was in our case, that the camera is the main limitation of the ability to report a SBP, because using a magnification sufficient to resolve the fine features results in the largest features not fitting in the camera aperture. This can be overcome in a multi-

shot geometry by using multiple FT^{-1} lenses with different magnifications to recover all the features, and can be overcome in a single-shot geometry by using a larger camera array or an array with smaller pixels so that large and fine features can be simultaneously recovered.

The detector face of the CCD camera we used was $8.5\text{mm}\times 6.5\text{mm}$, with pixels which are $6.7\mu\text{m}$ square. The design of the USAF 1951 target is such that cameras are not able to simultaneously see the entire range of the largest features on the 1951 USAF target and also resolve the smallest features. Because the detector was rectangular and not square, we could not capture on it all of the largest horizontal and vertical features in the target simultaneously, while maintaining a magnification which would allow us to resolve the finest features in the target. We were able to capture vertical features as large as 1.1 lp/mm , but horizontal features from only 2 lp/mm . The performance of our OPA imaging system in the horizontal direction should not differ from the vertical direction, but, because we were limited by the size of the detector, we could not compare the performances for the largest features on the target in the image.

5.4 Conclusions

Taking advantage of recent advances in the engineering of high-power femtosecond regeneratively amplified laser system, we performed OPA amplification of an image utilizing the Fourier-transform plane as the plane of interaction. We OPA amplified a complex image both with and without wavelength-downconversion (frequency-upconversion), achieving two orders of magnitude of amplification across a large spread of spatial frequencies in the input image. This amplification and wavelength conversion occurred simultaneously over more than an order of magnitude of spatial

frequency content in both the horizontal and vertical dimensions. This appears to be the most complex object ever imaged using OPA.

CHAPTER 6

SPATIAL FILTERING DURING OPA IMAGING

6.1 Introduction to Image Processing

The Fourier plane interaction allows for image processing to be performed. Computational image processing is generally performed on the Fourier transform of an image. Two of the most basic image processing techniques are low-pass frequency filtering, which is used to remove noise from a signal, and band-pass spatial frequency filtering, which allows removal of a constant background, commonly referred to as a DC term because of the common occurrence of signal in electrical engineering.

Image processing generally refers to any manipulation of an image. It is often performed by computers during post processing. Image processing can be used for things as simple as enlarging an image, noise filtering and contrast alteration. It is also used for much more complicated processes such as facial recognition and image registration. Image processing is a well developed field of study as it has so many uses. Optical Parametric Amplification for imaging allows for some all laser real time image processing, where some of these techniques can be performed without the use of any computer post-processing.

6.2 Real-Time Spatial Filtering as Image Processing using Nonlinear Optics

6.2.1 Spatial Overlap for Image Processing

There are two mechanisms by which image processing occurs during OPA. First, the nonlinear interaction can only occur when the pump beam and the seed beam spatially overlap. The pump beam therefore acts as a physical aperture on the seed beam. As a

result, the spatial distribution of the pump beam can be made to overlap with different regions of the seed beam and will act as an aperture on the region of the seed beam it overlaps with.

The configuration used for imaging will have further effects on the output image. In the real image plane geometry, the pump beam acts as a physical aperture on the input image, and the image which can be recovered is limited by the size of the pump beam (or the lateral dimensions of the crystal). With the Fourier plane as the plane of interaction, a Gaussian pump beam will cause there to be a non-uniform amplification across the spatial frequency spectrum. The highest spatial frequencies, which are furthest from the center in the Fourier plane, will be in the wings of the Gaussian pump beam and will not experience as great amplification as the low spatial frequencies. The Fourier plane interaction necessarily includes imaging through a low-pass filter, and to recover a complex image requires having a pump beam of large enough lateral dimensions to allow the desired portion of the spatial frequency spectrum through this filter.

6.2.2 Phase matching for Image Processing

The second mechanism which allows image processing to occur during the nonlinear interaction is phase matching. Phase matching allows for only wave vectors which are travelling in a specific direction to experience the nonlinear interaction. In a uniaxial crystal, phase matching will occur along a ring which is concentric about the pump beam direction. Because ultrafast optical pulse are made up of multiple frequencies, the phase matching across the entire pulse will either make up a disk centered around the pump beam, or a thick ring. The pump beam angle relative to the crystal optical axis and the central wavelength of the seed beam will determine whether

phase matching will occur in a disk or on a ring. In either case, the image will be modified because of this phase matching, which is considered image processing.

In order for image processing to be useful during nonlinear optical imaging, it must be useful and controllable. We have studied the effects of each of these mechanisms when the Fourier plane is the plane of interaction, and have found useful and practical image processing to be possible both theoretically and experimentally.

Using the Fourier plane for the interaction does not change either of the requirements for nonlinear interactions, but it changes the effect of both the aperture effect and the phase matching effect. Each of these effects in the real-image interaction plane is well understood. The aperture effect in the real-image plane has the effect of inserting a physical aperture into the beam. Only the portions of the seed beam which overlap with the pump beam will undergo the nonlinear interaction. In order to apply the process to complex images with the real-image plane as the plane of interaction, a large pump beam must be used. A large beam diameter will by definition be at a lower intensity than an equally energetic pump beam at a smaller diameter. When using OPA as the nonlinear interaction, this decrease in intensity will cause a significant loss in the potential gain from the interaction. However, it is necessary for the interaction to cover the entire image. Studies using the real image plane have been limited by this fact to studying small features.

6.2.3 Image Processing using the Real Image Plane Geometry

The influence of the phase matching interaction in the real image plane was discussed by Lantz, et al. when they defined the spatial frequency transfer function. That study utilized pulses which were tens of picoseconds long, so that they were narrowband

in spectral frequency content. Because they had only a narrow spectrum, as was discussed in section 1.2.3.1, they utilized only a very narrow phase matching bandwidth. Their study focused on the effect of rotating the crystal around the direction where perfect phase matching would occur. They found that as they rotated the crystal, the portion of the image which was in greatest contrast could be switched between the center of an image and its edges. This edge enhancement was performed on the numeral 4, so that the figure or its outline could be clearly seen depending on the crystal orientation.

6.2.4 Image Processing using the Fourier Plane Geometry

The Fourier plane results in the exact opposite effects as using the real imaging plane. The spatial overlap between the pump and the seed beam define the spatial frequency transfer function. The phase matching condition dictates which spatial regions of the image will be phase matched. This somewhat surprising conclusion is born out by theory and makes sense once it is thoroughly examined.

That the physical overlap between the pump beam and the seed beam determining the spatial frequency transfer function makes sense. The Fourier transform of the image is the spatial frequency distribution, and so only the spatial frequencies which are within the profile of the pump beam can experience the nonlinear interaction. One immediate result arises from the use of the USAF 1951 target is that any imaging with the Fourier transform interaction will have softened edges. With a round pump beam, the spatial overlap between the pump beam and the seed image leads to a straightforward low-pass spatial frequency filtering. The USAF1951 image target has a series of hard-edge steps where the transmission goes from 0 to 1 abruptly, with essentially no transmission gradient between these regions. These hard edges correspond to an infinite spatial

frequency. While this is non-physical, the very rapid changes between light and dark regions will correspond to very high spatial frequencies. These high spatial frequencies will not lie within the crystal aperture, and therefore there will necessarily be some softening of the edges as a result of using the Fourier plane as the interaction plane.

To understand the aperture effect imposed by the phase matching condition requires first understanding the spatial frequency transfer function in the real image geometry. Phase matching in the real image geometry results in certain spatial frequencies being passed. If the crystal is oriented at normal incidence, low spatial frequencies are passed. As the crystal is rotated, higher spatial frequencies are passed and lower spatial frequencies are suppressed. The same physical mechanism is present when the Fourier transform plane is used to conduct the interaction, although the results are quite dissimilar. The results are that phase matching allows for portions of the image near the center of the image to be passed when the crystal is near normal incidence and the interaction allows for features farther from the center to undergo the nonlinear interaction as the crystal is rotated. This occurs because wave vector distribution of the Fourier transform of the image is the image itself. Therefore, when low spatial frequencies are passed, the result is that features near the center of the image are passed. When higher spatial frequencies are passed in a ring about the central spatial frequency, the interaction acts like a doughnut shaped aperture inserted into the beam path, allowing only spatial features which are the same distance from the center of that image to pass.

6.3 Theoretical Investigation of Spatial Filter Processing

Image processing is usually done as post-processing using a computer. However, because of the unique nature of these interactions, we can perform all-optical image

processing to output a processed image directly from the experiment. Before beginning the demonstration of all optical image processing, however, we investigated the process using a computer. Before we examine image processing, we show in Figure 27 the simulation of the USAF1951 target image as well as its Fourier spectrum.

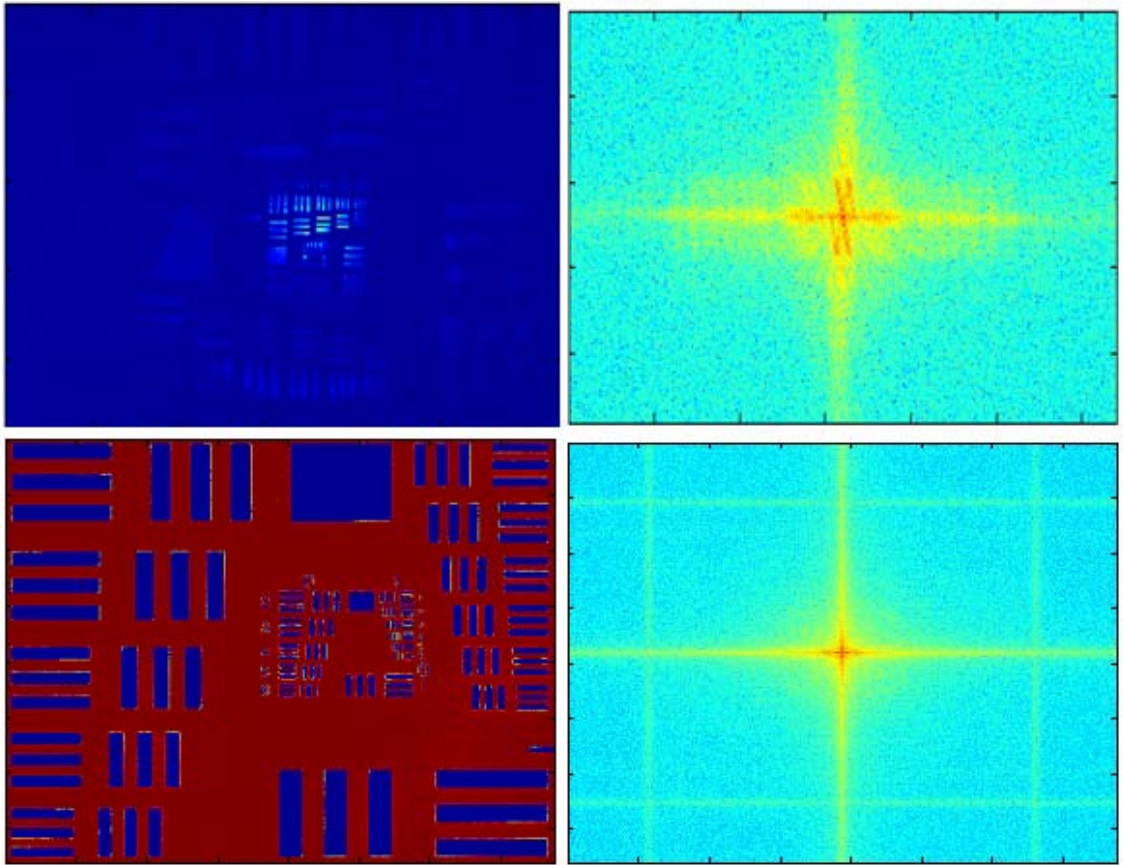


Figure 27. An image of the USAF 1951 target and its Fourier spectrum in log scale with a simulation of the USAF 1951 target and its Fourier spectrum in log scale.

6.3.1 Spatial Overlap of the Fourier Transform and a Gaussian Pump Beam

The Fourier spectrum is accessible at the focal plane of the imaging lens (see Appendix A). The interaction between the Fourier spectrum and the pump beam is therefore a Fourier filtering process. In order to understand this process, we examined how the Fourier spectrum interacted with different types of pump beams. Figure 28 demonstrates the effect of a large versus a small Gaussian pump beam which is symmetric in the x and y directions interacting with this Fourier spectrum. This demonstrates the low-pass filtering which occurs when a small pump beam is used.

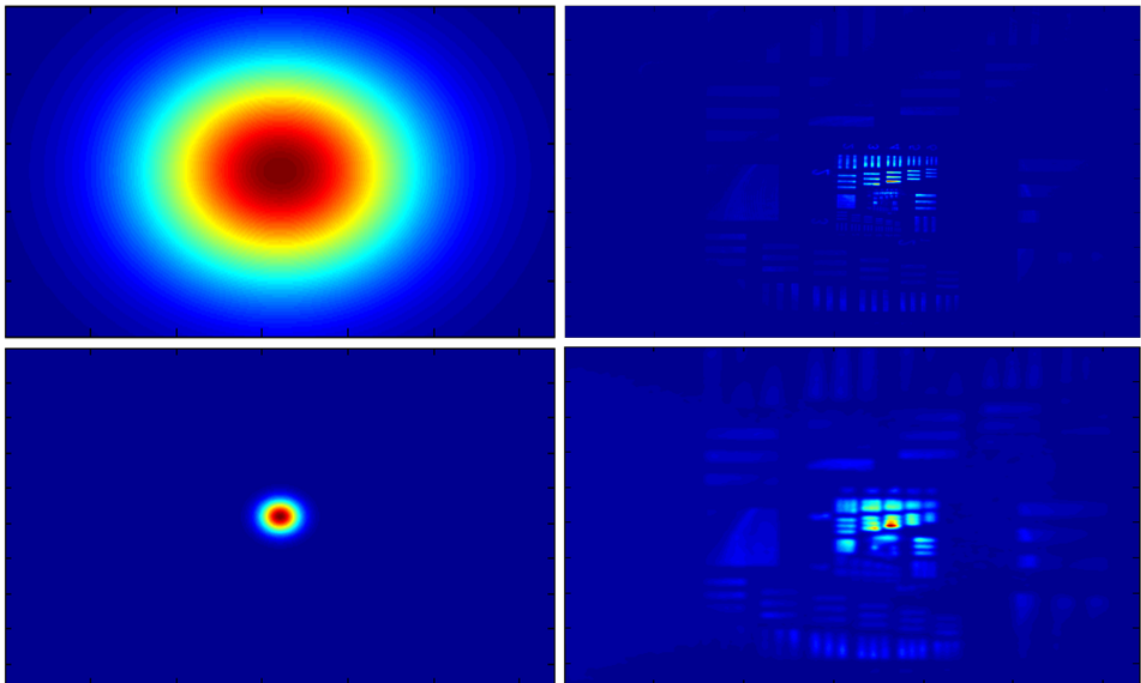


Figure 28. The effect of a large versus small Gaussian pump beam.

6.3.1 Spatial Overlap of the Fourier Transform and a Cylindrical Pump Beam

The Fourier plane interaction will allow not only for using a low-pass filter, as we demonstrated in section 6.3.1. It also allows for the use of different shaped pump beams to perform more advanced Fourier filtering interactions. A spatial light modulator[78] is capable of making a laser beam into essentially any shape by applying a variable phase mask to the beam. However, even without such a powerful optical component, some rudimentary image processing can be displayed. One of the most straightforward pump beam shapes to make is the cylinder, which can be done simply by using a cylindrical lens in the beam path. To see the anticipated effect of using a cylindrical pump beam, we again performed simulations, shown in Figure 29.

The results show that a pump beam which is thicker will allow more of the transverse spatial frequencies to be properly imaged, which a thinner pump beam will allow for only a much narrower transverse spectrum. This is shown in Figure 29 by the decrease in the resolution of the vertical features as the pump beam thickness is decreased. Using a pump beam which is too small in the lateral dimension will also decrease the resolution in that direction. However, it is not necessary to overfill the Fourier spectrum in the lateral dimension in order to achieve significant discrimination between the lateral and transverse directions. It is also worth noting that using a horizontal pump beam results in a blurring of *horizontal* features, so that only *vertical* features can be clearly seen after using such a pump beam.

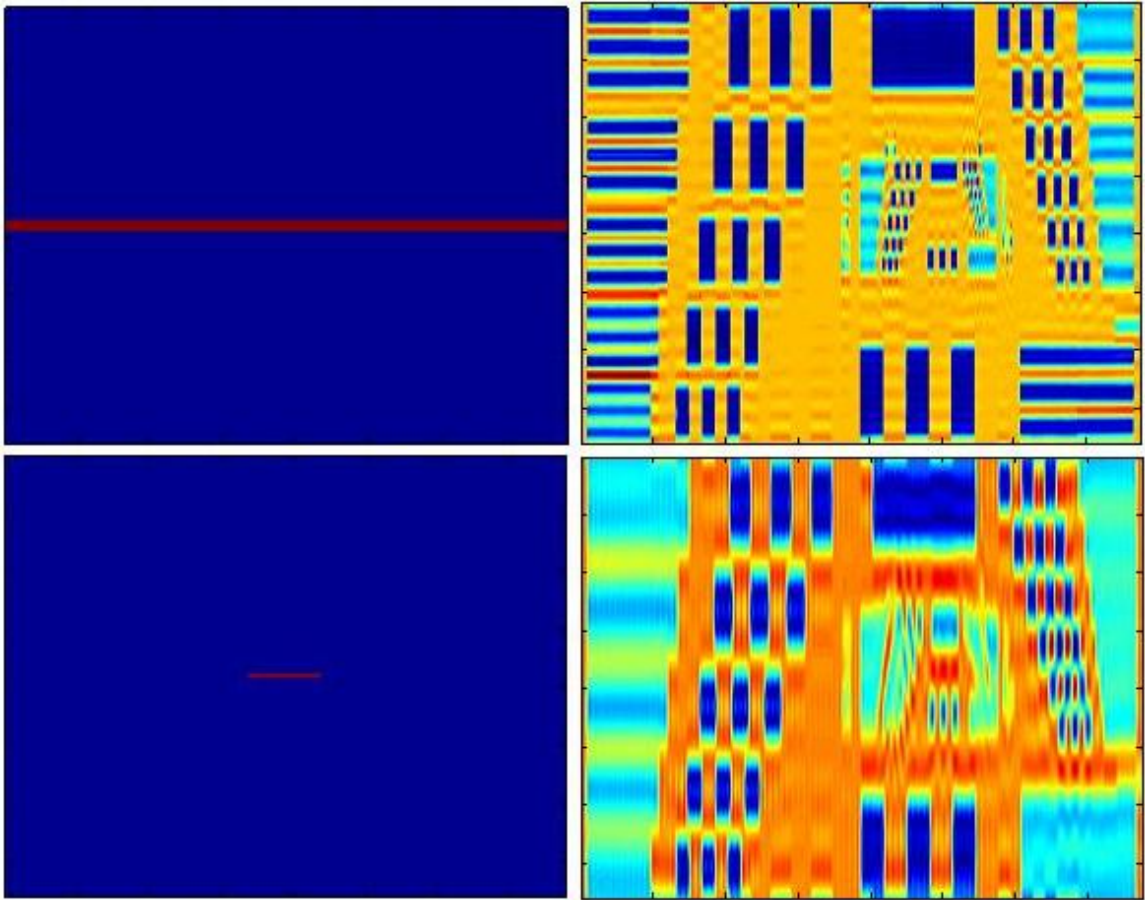


Figure 29. A thick, long cylindrical pump beam and a thin, short beam.

This final point is practically important from an experimental consideration. Using a cylindrical focus significantly decreases the amount of intensity in a beam, as compared with using a spherical focus. Because OPA is dependant on the intensity of the pump beam, a bema which is smaller when it passes through the cylindrical lens will focus to a smaller lateral size. Having the lateral dimension as small as possible will be experimentally very advantageous, as we demonstrate in section 6.4.1. Moreover, having a focus which is tight in the lateral dimension will lead to a better demonstration of the image processing capabilities of OPA imaging by washing out the transverse dimensions to a much greater extent.

6.4 Experimental Demonstration of Spatial Filter Image Processing

In order to demonstrate these spatial filtering considerations, we shaped a pump beam using a pair of positive focus cylindrical lenses. A cylindrical lens focus is not intense enough to generate supercontinuum in air (see section 1.2.2.4) and so a pair of positive focal length cylindrical lenses can be used. It is still important to use a pair of lenses because the pump beam, whether it is Gaussian or cylindrical, must be well collimated in order to maximize the resolution in the desired dimension (see section 4.5).

6.4.1 Demonstration of Spatial Filtering by Pump and Seed Overlap

We used a 500mm cylindrical focal length lens paired with a 100mm cylindrical focal length lens to generate a line pump beam. The results of a vertical pump beam are shown in Figure 30. In this figure, the horizontal features are resolvable from 1.0 lp/mm to 5.66 lp/mm, while in the vertical dimension only the elements at 1.0 lp/mm and 1.12 lp/mm can be resolved. With the decrease in intensity from the cylindrical lens, the amplification at the seed wavelength decreases significantly. As a result, the amount of

amplification at the seed wavelength is of order unity, and is insufficient to record the amplified signal image and necessarily distinguish it from the initial unamplified seed image. As a result, the processed images are all images of the wavelength-shifted DFG beam.

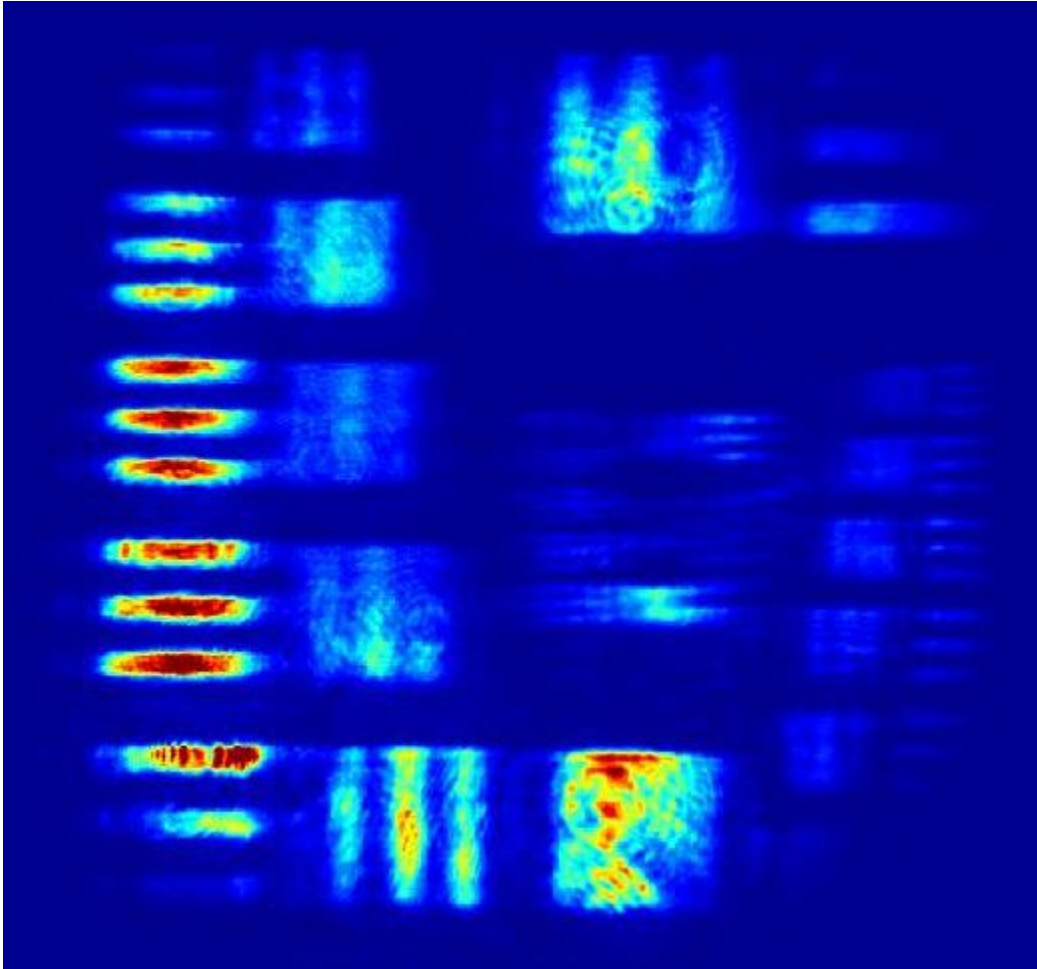


Figure 30. A spatially filtered USAF1951 target where horizontal features are preserved while vertical features beyond the largest are not resolvable.

6.4.2 Demonstration of Phase matching as a Ring-Shaped Aperture

The phase matching condition also leads to image processing. This is a fundamentally different type of image processing than the overlaps leads to, and the result is that as the crystal is rotated about its axis, the portion of the image which can be seen evolves from a small disk centered at the middle of the image to a ring of increasing diameter, but of decreasing thickness. This is shown in Figure 31, which is a display of the image as it is rotated through 0.60° . The first image of this series was taken with the crystal rotated so that the back reflection was just below normal incidence, at 0.16° . The crystal was rotated up, so that the back reflection went through normal incidence at 0° and the final image in the sequence was taken at an 0.54° crystal angle.

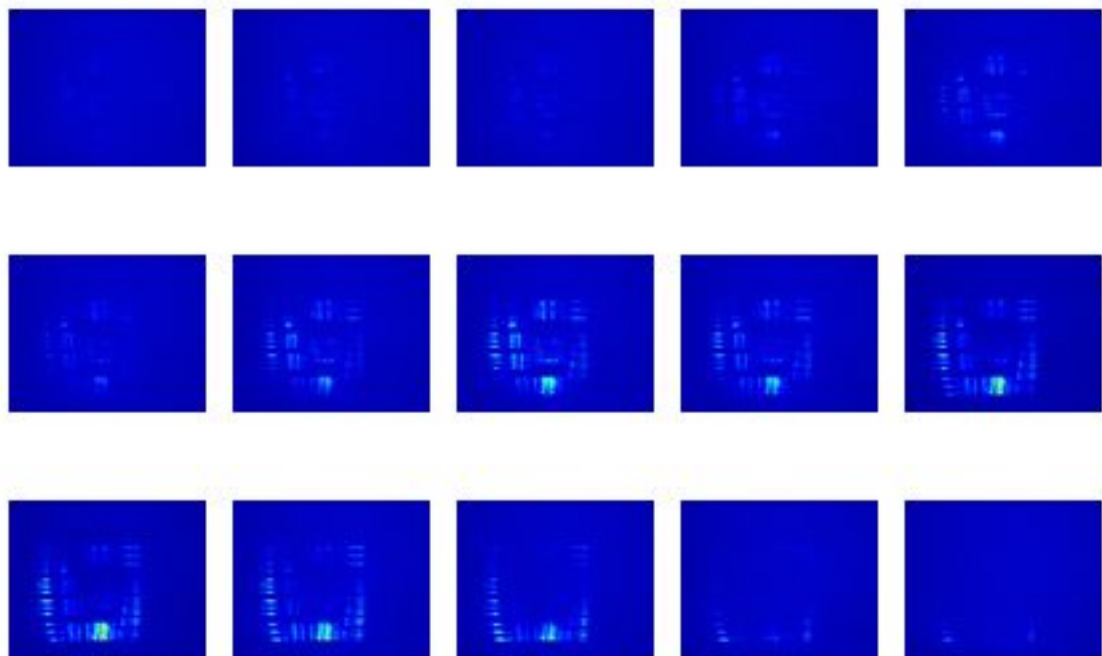


Figure 31. A sequence of images showing the ring-shaped aperture.

APPENDIX A

THE PROOF THAT THE FOCUS OF A LENS IS THE FOURIER TRANSFORM PLANE

It is a fundamental principle of Fourier Theory that a signal and the signals Fourier Transform must contain the same information. A spatial distribution, such as an image, will have a Fourier Transform which will contain the same information, which is the spatial frequency distribution. Because these two distributions contain the same information, we can perform Optical Parametric Amplification on either the image or on the Fourier transform of the image, with the same result, namely amplification of the input image.

This is extremely useful because obtaining either the real space image or the Fourier transform is as simple as placing a lens between the object and the non-linear medium. While the Fourier Transform is commonly associated with computer manipulation of a signal, it turns out that in optics, accessing the Fourier plane is simple. When the lens is placed so that the lens maker's formula is satisfied, the real image will be imparted on the nonlinear medium. When the distance between the lens and the image is f , and the distance between the lens and the nonlinear medium is also f , the Fourier transform of the image will be placed on the nonlinear medium. The Fourier transform of an object one focal length before a lens occurs one focal length after the lens.

To demonstrate this, we follow Goodman[64]. Consider a thin lens with a maximum (on axis) thickness of Δ_0 and a thickness at a transverse position $\Delta(x, y)$ as shown in Figure 32. The only effect of a thin lens is to introduce a phase delay to an

incident wave front by an amount equal to the transverse thickness. A wave with coordinates (x,y) will have a phase delay given by

$$\phi(x, y) = kn\Delta(x, y) + k[\Delta_0 - \Delta(x, y)] \quad (\text{A.1})$$

where n is the index of refraction of the lens material.

The lens can, therefore, be considered as a phase transformation of

$$t_L = e^{ikn\Delta(x,y)} e^{ik\Delta_0} e^{-ik\Delta(x,y)} \quad (\text{A.2})$$

The first term is the phase delay introduced which the beam receives from the lens. The second and third terms are the phase delay which the lens accumulates upon propagation through free space after the lens.

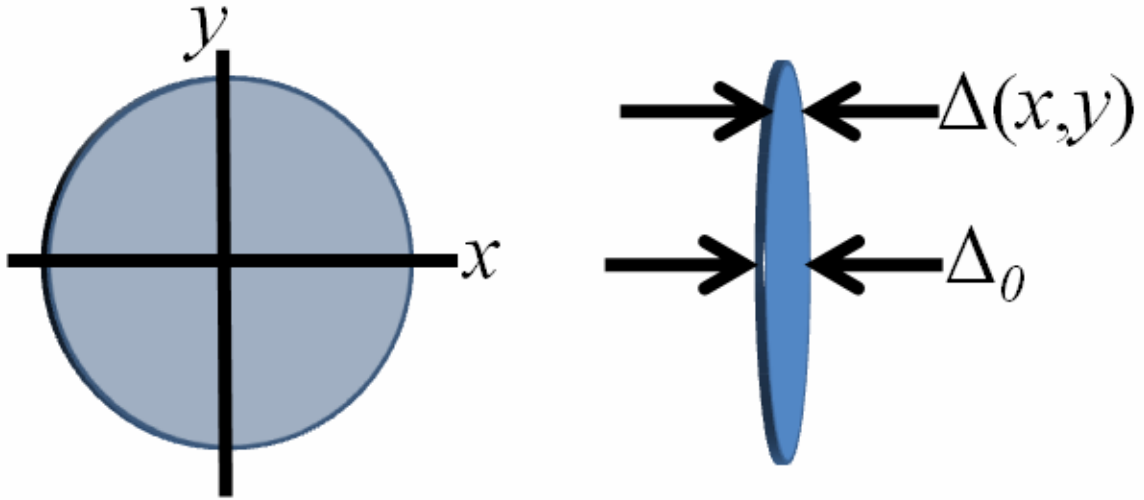


Figure 32. The thickness of a lens depends on the transverse position across the lens.

We consider the lens as comprised of three sections A, B, and C, where A is the portion of the lens with a curvature on the left and a flat region on the right, B the middle where both regions are flat, and C is the region which is flat on the left and curved on the right. In this manner, we can determine that the thickness $\Delta(x, y)$ is given by

$$\Delta(x, y) = \Delta_0 - R_A \left(1 - \sqrt{1 - \frac{x^2 + y^2}{R_A^2}} \right) + R_C \left(1 - \sqrt{1 - \frac{x^2 + y^2}{R_C^2}} \right) \quad (\text{A.3})$$

When x and y are small, we can expand the square roots in equation (A.3), which technically is referred to as the Paraxial Approximation. Due to the similarity of the square root terms, under the paraxial approximation, equation (A.3) simplifies by combining like terms to

$$\Delta(x, y) = \Delta_A + \Delta_B + \Delta_C - \frac{x^2 + y^2}{2} \left(\frac{1}{R_A} - \frac{1}{R_C} \right) \quad (\text{A.4})$$

We can apply this to the phase transformation (A.2)

$$t_L = e^{ik\Delta_0} \exp \left(-ik(n-1) \frac{x^2 + y^2}{2} \left(\frac{1}{R_A} - \frac{1}{R_C} \right) \right) \quad (\text{A.5})$$

This formula can be simplified by rewriting the radius of curvature formula in terms of the lens focal length. The simplest formula can be written in terms of the inverse focal length formula $1/f = (n-1)(1/R_A - 1/R_C)$. The simplified formula is

$$t_L = e^{ik\Delta_0} e^{-i \frac{k}{2f} (x^2 + y^2)} \quad (\text{A.6})$$

The phase transformation describes the form a plane wave will have upon exiting the lens, so that $U_{OUT} = U_{IN} t_L$. To determine the distribution at a later plane, we use the Fresnel propagation formula.

$$U(x, y) = \frac{e^{ikz}}{i\lambda z} e^{i \frac{k}{2z} (x^2 + y^2)} \int \int_{-\infty}^{\infty} \left(U(\xi, \eta) e^{i \frac{k}{2z} (\xi^2 + \eta^2)} \right) e^{-i \frac{2\pi}{\lambda z} (x\xi + y\eta)} d\eta d\xi \quad (\text{A.7})$$

We propagate U_{OUT} using (A.7) to the focal plane, located f behind the lens,

$$U(x, y) = \frac{\exp \left(i \frac{k}{2f} (u^2 + v^2) \right)}{i\lambda f} \int \int_{-\infty}^{\infty} \left(U_{OUT}(x, y) e^{i \frac{k}{2f} (x^2 + y^2)} \right) e^{-i \frac{2\pi}{\lambda f} (xu + yv)} dx dy \quad (\text{A.8})$$

The exponential in the double integral of (A.8) and the exponential in (A.6) cancel, so that substituting (A.6) into (A.8) yields

$$U(x, y) = \frac{\exp\left(i\frac{k}{2f}(u^2 + v^2)\right)}{i\lambda f} \int_{-\infty}^{\infty} \int_{-\infty}^{\infty} U_{IN}(x, y) e^{-i\frac{2\pi}{\lambda f}(xu + yv)} dx dy \quad (\text{A.9})$$

The amplitude distribution at the focal plane is proportional to the Fourier transform. There is, however, the quadratic phase factor in (A.9) which precedes the Fourier transform. Next, we will show that when the image is plane at a distance $d=f$ in front of the lens, this term exactly cancels out and that a lens takes the distribution at $d=f$ before the lens and reproduces the Fourier transform of that distribution at $f=d$ behind the lens.

The Fourier transform of the object at a distance d before the lens, F_O , is related to the Fourier transform of the light incident upon the lens, F_L , by the transfer function for Fresnel propagation

$$H(f_x, f_y) = e^{ikz} e^{-i\pi\lambda d(f_x^2 + f_y^2)} \quad (\text{A.10})$$

So that

$$F_L(f_x, f_y) = F_O(f_x, f_y) e^{ikz} e^{-i\pi\lambda d(f_x^2 + f_y^2)} \quad (\text{A.11})$$

Rewriting (A.9) in terms of F_L yields

$$U(x, y) = \frac{\exp\left(i\frac{k}{2f}(u^2 + v^2)\right)}{i\lambda f} F_L\left(\frac{u}{\lambda f}, \frac{v}{\lambda f}\right) \quad (\text{A.12})$$

Finally, at long last, substituting (A.11) into (A.12) gives

$$U(x, y) = \frac{\exp\left(i \frac{k}{2f} \left(1 - \frac{d}{f}\right) (u^2 + v^2)\right)}{i\lambda f} F_o\left(\frac{u}{\lambda f}, \frac{v}{\lambda f}\right) \quad (\text{A.13})$$

This term will reduce to the Fourier transform when the phase factor vanishes.

When $d=f$, and only when $d=f$, the phase factor term identically vanishes. Therefore a thin lens will reproduce at its back focus the Fourier transform of the image at its front focus.

APPENDIX B

DESCRIPTION OF THE USAF 1951 TARGET

The image target which we used throughout our experiments was the USAF 1951 resolution test target, designed to conform to MIL-STD-150A[77]. This target is designed so that it is not possible to both view the largest features while simultaneously resolving the smallest features. The target consists of transparent bars on an opaque background, where opaque is defined as having an optical density of at least 2.00 greater than transparent. These are arranged in groups, where each group has 6 elements. Each set of bars is three transparent bars of length $0.5/x$ and width $2.5/x$. The gap between each pair of bars is $0.5/x$. Each element set consists is one set of vertical bars and one set of horizontal bars, with a $1.0/x$ spacing between the vertical and horizontal features. Here, x is the number of lines per millimeter for that particular element. The number of lines per millimeter is related to the group number and the element number by

$$x = 2^{\text{Group}+(\text{Element}-1)/6} \quad (\text{B.1})$$

These features are arranged so that each pair of two groups is contained within the larger sets of two groups. The schematic is given by Figure 33[79]. While that schematic displays groups -2 and -1 as the largest features, the target used in these experiment had group 0 as the largest group. The target that we used in these experiments was from Newport Corporation[80]. This target was fabricated of opaque chrome on a glass substrate. The opaque chrome attenuates to OD 2.0 relative to the clear lines. The glass in the target does cause a slight temporal delay to be introduced to the beam which must be accounted for when temporally overlapping the image seed beam with the pump beam.

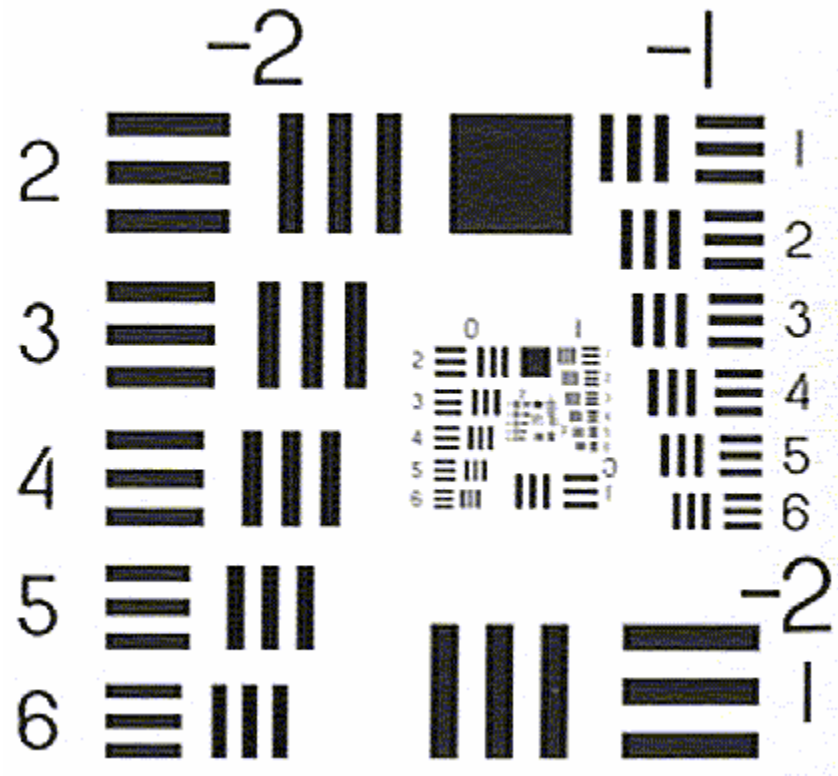


Figure 33. Schematic of the USAF-1951 resolution test target.

REFERENCES

1. A. Consoli, V. Chauhan, J. Cohen, L. Xu, P. Vaughan, F. J. Lopez-Hernandez, and R. Trebino, "Retrieving Two Pulses Simultaneously and Robustly Using Double-Blind FROG," in *Frontiers in Optics*, 2010), FThD8.
2. L. Xu, "Measurement of complex ultrashort laser pulses using frequency-resolved optical gating," (Georgia Institute of Technology, Atlanta, 2009).
3. P. M. Vaughan and R. Trebino, "Optical-parametric-amplification imaging of complex objects," *Opt. Express* **19**, 8920-8929 (2011).
4. P. Vaughan and R. Trebino, "Demonstration of Real-Time All-Optical Image Processing Using Optical Parametric Amplification of Complex Objects," in *Frontiers in Optics*, 2011),
5. B. K. Garside and T. K. Lim, "Laser mode locking using saturable absorbers," *Journal of Applied Physics* **44**, 2335 - 2342 (1973).
6. R. Trebino, *Frequency-Resolved Optical Gating: The Measurement of Ultrashort Laser Pulses* (Kluwer Academic Publishers, Boston, 2002).
7. M. Maier, W. Kaiser, and J. A. Giordmaine, "Intense Light Bursts in the Stimulated Raman Effect," *Phys. Rev. Lett.* **17**, 1275 (1966).
8. F. Krausz, M. E. Fermann, T. Brabec, P. F. Curley, M. Hofer, M. H. Ober, C. Spielmann, E. Wintner, and A. J. Schmidt, "Femtosecond solid-state lasers," *IEEE Journal of Quantum Electronics* **28**, 2097 - 2122 (1992).
9. M. Hirasawa, N. Nakagawa, K. Yamamoto, R. Morita, H. Shigekawa, and M. Yamashita, "Sensitivity improvement of spectral phase interferometry for direct electric-field reconstruction for the characterization of low-intensity femtosecond pulses," *Applied Physics B: Lasers and Optics* **74**, s225-s229 (2002).
10. E. Zeek, A. P. Shreenath, M. Kimmel, and R. Trebino, "Simultaneous Automatic Calibration and Direction-of-Time-Ambiguity Removal in Frequency-Resolved Optical Gating," *Appl. Phys. B* **B74**, S265-271 (2002).
11. D. Keusters, H.-S. Tan, P. O'Shea, E. Zeek, R. Trebino, and W. S. Warren, "Relative-phase ambiguities in measurements of ultrashort pulses with well-separated multiple frequency components," *J. Opt. Soc. Amer. B* **20**, 2226-2237 (2003).
12. J.-H. Chung and A. M. Weiner, "Ambiguity of ultrashort pulse shapes retrieved from the intensity autocorrelation and power spectrum," *IEEE J. Sel. Top. Quant. Electron.* **7**, 656-666 (2001).
13. K. W. DeLong, D. N. Fittinghoff, R. Trebino, B. Kohler, and K. Wilson, "Pulse Retrieval in Frequency-Resolved Optical Gating Based on the Method of Generalized Projections," *Optics Letters* **19**, 2152-2154 (1994).
14. R. L. Fork, O. E. Martinez, and J. P. Gordon, "Negative dispersion using pairs of prisms," *Opt. Lett.* **9**, 150-152 (1984).
15. A. Michelson and E. Morley, "On the Relative Motion of the Earth and the Luminiferous Ether," *American Journal of Science*, 333-345 (1887).

16. C. Iaconis and I. A. Walmsley, "Self-Referencing Spectral Interferometry for Measuring Ultrashort Optical Pulses," *IEEE J. Quant. Electron.* **35**, 501-509 (1999).
17. C. Dorrer and I. A. Walmsley, "Accuracy criterion for ultrashort pulse characterization techniques: application to spectral phase interferometry for direct electric field reconstruction," *J. Opt. Soc. Am. B* **19**, 1019-1029 (2002).
18. J. Herrmann, "Theory of Kerr-lens mode locking: role of self-focusing and radially varying gain," *J. Opt. Soc. Am. B* **11**, 498-512 (1994).
19. E. P. Ippen, "Principles of passive mode locking," *Applied Physics B: Lasers and Optics* **58**, 159-170 (1994).
20. P. F. Moulton, "Spectroscopic and laser characteristics of Ti:Al₂O₃," *J. Opt. Soc. Am. B* **3**, 125-133 (1986).
21. E. Gulevich, S. S. Dvornikov, A. Kachinsky, I. Kalitukho, A. L. Protasenya, and V. A. Tugbayev, "Current state and prospects for tunable titanium-sapphire lasers," in (SPIE, 1994), 102-104.
22. G. Vaillancourt, T. B. Norris, J. S. Coe, P. Bado, and G. A. Mourou, "Operation of a 1-kHz pulse-pumped Ti:sapphire regenerative amplifier," *Opt. Lett.* **15**, 317-319 (1990).
23. O. E. Martinez, J. P. Gordon, and R. L. Fork, "Negative group-velocity dispersion using refraction," *J. Opt. Soc. Am. A* **1**, 1003-1006 (1984).
24. S. Akturk, X. Gu, M. Kimmel, and R. Trebino, "Extremely simple single-prism ultrashort-pulse compressor," *Opt. Express* **14**, 10101-10108 (2006).
25. E. B. Treacy, "Optical pulse compression with diffraction gratings," *IEEE Journal of Quantum Electronics* **5**, 454 - 458 (1969).
26. J. M. Manley and H. E. Rowe, "Some General Properties of Nonlinear Elements-Part I. General Energy Relations," in *Proceedings of the Institute of Radio Engineers*, 1956), 904-913.
27. P. O'Shea, M. Kimmel, X. Gu, and R. Trebino, "Highly simplified device for ultrashort-pulse measurement," *Optics Letters* **26**, 932-934 (2001).
28. K. W. DeLong, R. Trebino, J. Hunter, and W. E. White, "Frequency-Resolved Optical Gating With the Use of Second-Harmonic Generation," *J. Opt. Soc. Amer. B* **11**, 2206-2215 (1994).
29. R. R. Alfano and S. L. Shapiro, "Observation of Self-Phase Modulation and Small-Scale Filaments in Crystals and Glasses," *Physical Review Letters* **24**, 592 (1970).
30. J. Dudley, X. Gu, X. Lin, M. Kimmel, E. Zeek, P. O'Shea, R. Trebino, S. Coen, and R. S. Windeler, "Cross-correlation frequency resolved optical gating analysis of broadband continuum generation in photonic crystal fiber: simulations and experiments," *Opt. Expr.* **10**, 1215-1221 (2002).
31. N. Aközbek, M. Scalora, C. M. Bowden, and S. L. Chin, "White-light continuum generation and filamentation during the propagation of ultra-short laser pulses in air," *Optics Communications* **191**, 353-362 (2001).
32. D. N. Nikogosyan, "Beta barium borate (BBO)," *Applied Physics A: Materials Science & Processing* **52**, 359-368 (1991).
33. V. G. Dmitriev, G. G. Gurzadyan, and D. N. Nikogosyan, *Handbook of Nonlinear Optical Crystals*, Springer Series in Optical Sciences (Springer, 1999).

34. E. Lantz, L. Han, A. Lacourt, and J. Zyss, "Simultaneous angle and wavelength one-beam noncritical phase matching in optical parametric amplification," *Optics Communications* **97**, 245-249 (1993).
35. V. Chauhan, "Pulse Compression and Dispersion Control in Ultrafast Optics," (Georgia Institute of Technology, Atlanta, 2010).
36. A. Freiberg and P. Saari, "Picosecond Spectrochronography," *JQE QE-19*, 622-630 (1983).
37. X. Gu, M. W. Kimmel, E. Zeek, P. O'Shea, R. Trebino, and R. S. Windeler, "Cross-correlation frequency-resolved-optical-gating measurements of ultrabroadband continuum from microstructure optical fiber," in *Ultrafast Phenomena XIII*, Thirteenth International Conference on Ultrafast Phenomena. Technical Digest (TOPS Vol.72) (Opt. Soc. America, 2002), 277-278.
38. K. W. DeLong, R. Trebino, and D. J. Kane, "Comparison of Ultrashort-Pulse Frequency-Resolved-Optical-Gating Traces for Three Common Beam Geometries," *J. Opt. Soc. Amer. B* **11**, 1595-1608 (1994).
39. K. W. DeLong, R. Trebino, and W. E. White, "Simultaneous Recovery of Two Ultrashort Laser Pulses from a Single Spectrogram," *J. Opt. Soc. Am. B* **12**, 2463-2466 (1995).
40. B. Seifert, H. Stolz, and M. Tasche, "Nontrivial ambiguities for blind frequency-resolved optical gating and the problem of uniqueness," *J. Opt. Soc. Am. B* **21**, 1089-1097 (2004).
41. Y. Mairesse and F. Quere, "Frequency Resolved Optical Gating for Complete Reconstruction of Attosecond Bursts," *Physical Review A* **71**, 011401 (2005).
42. P. M. Fauchet, W. L. J. Nighan, and R. Trebino, "Characterization of Ultrashort Laser Pulses by the Method of Self-Diffraction," in *First International Laser Science Conference*, 1985),
43. D. J. Kane and R. Trebino, "Single-Shot Measurement of the Intensity and Phase of a Femtosecond Pulse Using the Optical-Kerr Effect," in *Nonlinear Optics*, (1992).
44. D. J. Kane and R. Trebino, "Single-Shot Measurement of the Intensity and Phase of a Femtosecond Pulse," in *Ultrafast Phenomena*, (1992).
45. A. Brun, P. Georges, G. LeSaux, and F. Salin, "Single-Shot Characterization of Ultrashort Light Pulses," *J. Phys. D.* **24**, 1225-1233 (1991).
46. K. W. DeLong, R. Trebino, and D. J. Kane, "Measurement of the Intensity and Phase of a Single Ultrashort Pulse: A Simple and General Technique," in *Laser Spectroscopy XI*, L. A. Bloomfield, T. F. Gallagher, and D. J. Larson, eds. (American Institute of Physics, Woodbury, NY, 1993), pp. 300-301.
47. S. Linden, H. Giessen, and J. Kuhl, "XFROG-a new method for amplitude and phase characterization of weak ultrashort pulses," *Physica Status Solidi B Conference Title: Phys. Status Solidi B (Germany)* **206**, 119-124 (1998).
48. M. Born and E. Wolf, *Principles of Optics: Electromagnetic Theory of Propagation, Interference and Diffraction of Light* (Cambridge University Press, Cambridge, 1997).
49. J. E. Midwinter, "Image Conversion from 1.6 μ m to the Visible in Lithium Niobate," *Applied Physics Letters* **12**, 68-71 (1968).

50. E. Lantz and F. Devaux, "Parametric Amplification of Images: From Time Gating to Noiseless Amplification," *IEEE Journal of Selected Topics in Quantum Electronics* **14**, 635-648 (2008).
51. F. Devaux and E. Lantz, "Transfer function of spatial frequencies in parametric image amplification: experimental analysis and application to picosecond spatial filtering," *Optics Communications* **114**, 295-300 (1995).
52. F. Devaux and E. Lantz, "Parametric Amplification of a polychromatic image," *J Opt Soc Am B* **12**, 2245-2253 (1995).
53. E. Lantz and F. Devaux, "Parametric amplification of images," *Quantum and Semiclassical Optics: Journal of the European Optical Society Part B* **9**, 279-286 (1997).
54. F. Devaux, E. Lantz, A. Lacourt, D. Gindre, H. Maillotte, P. A. Doreau, and T. Laurent, "Picosecond parametric amplification of a monochromatic image," *Nonlinear Optics* **11**, 25-38 (1995).
55. D. Guthals and D. Sox, "Quantum Limited Optical Parametric Image Amplification," in *Proceedings of the International Conference on Lasers*, 1989), 808-816.
56. G. W. Faris and M. Banks, "Upconverting time gate for imaging through highly scattering media," *Opt. Lett.* **19**, 1813-1816 (1994).
57. A. H. Firester, "Image Upconversion: Part III," *J. Appl. Phys.* **41**, 703-710 (1970).
58. P. V. Avizonis, F. A. Hopf, D. W. Bomberger, S. F. Jacobs, A. Tomita, and K. H. Womack, "Optical Phase Conjugation in a lithium formate crystal," *Appl. Phys. Lett* **31**, 435-438 (1977).
59. L. Lefort and A. Barthelemy, "Revisiting optical phase conjugation by difference-frequency generation," *Opt. Lett.* **21**, 848-851 (1996).
60. F. Devaux, G. L. Tolguenac, and E. Lantz, "Phase conjugate imaging by type II parametric amplification," *Opt. Commun.* **147**, 309-313 (1998).
61. A. W. Lohmann, R. G. Dorsch, D. Mendlovic, Z. Zalevsky, and C. Ferreira, "Space-bandwidth product of optical signals and systems," *J Opt Soc Am A* **13**, 470-473 (1996).
62. F. Devaux, A. Mosset, E. Lantz, S. Monneret, and H. Le Gall, "Image Upconversion from the Visible to the UV Domain: Application to Dynamic UV Microstereolithography," *Appl. Opt.* **40**, 4953-4957 (2001).
63. J. S. Dam, C. Pedersen, and P. Tidemand-Lichtenberg, "High-resolution two-dimensional image upconversion of incoherent light," *Opt. Lett.* **35**, 3796-3798 (2010).
64. J. W. Goodman, *Introduction to Fourier Optics*, 2nd ed. (McGraw-Hill, New York, 1996).
65. J. A. Armstrong, N. Bloembergen, J. Ducuing, and P. S. Pershan, "Interactions between Light Waves in a Nonlinear Dielectric," *Physical Review* **127**, 1918-1939 (1962).
66. C. C. Wang and G. W. Racette, "Measurement of parametric gain accompanying optical difference frequency generation," *Applied Physics Letters* **6**, 169-171 (1965).
67. F. Zernike and J. E. Midwinter, *Applied Nonlinear Optics* (Wiley, New York, 1973).

68. J. Watson, P. Georges, T. Lépine, B. Alonzi, and A. Brun, "Imaging in diffuse media with ultrafast degenerate optical parametric amplification," *Opt. Lett.* **20**, 231-233 (1995).
69. R. W. Boyd, *Nonlinear Optics* (Academic Press, 2002).
70. N. P. Barnes and V. J. Corcoran, "Parametric generation processes: spectral bandwidth and acceptance angles. [Wave vector mismatch, Taylor series]," *Journal Name: Appl. Opt.*; (United States); *Journal Volume: 15:3*, *Medium: X*; *Size: Pages: 696-699* (1976).
71. A. Shirakawa and T. Kobayashi, "Noncollinearly phase-matched femtosecond optical parametric amplification with a 2000 cm⁻¹ bandwidth," *Applied Physics Letters* **72**, 147-149 (1998).
72. W. H. Louisell, A. Yariv, and A. E. Siegman, "Quantum Fluctuations and Noise in Parametric Processes. I," *Physical Review* **124**, 1646–1654 (1961).
73. V. Krylov, J. Gallus, U. P. Wild, A. Kalintsev, and A. Rebane, "Femtosecond noncollinear and collinear parametric generation and amplification in BBO crystal," *Applied Physics B: Lasers and Optics* **70**, 163-168 (2000).
74. J.-Y. Zhang, J. Y. Huang, and Y. R. Shen, *Optical Parametric Generation and Amplification* (Harwood Academic Publishers GmbH, Luxembourg, 1995).
75. A. P. Shreenath, "Measuring Broadband, Ultraweak, Ultrashort Pulses," *Dissertation* (Georgia Institute of Technology, Atlanta, 2005).
76. R. A. Andrews, "IR Image Parametric Up-Conversion," *IEEE Journal of Quantum Electronics* **QE-6**, 68-81 (1970).
77. "Military Standard Photographic Lenses," (1959).
78. S. D. Coomber, C. D. Cameron, J. R. Hughes, D. T. Sheerin, C. W. Slinger, M. A. G. Smith, and M. Stanley, "Optically addressed spatial light modulators for replaying computer-generated holograms," in (SPIE, 2001), 9-19.
79. E. F. Glynn, "USAF 1951 and Microcopy Resolution Test Charts and Pixel Profiles" (2002), retrieved June 08, 2011, <http://www.efg2.com/Lab/ImageProcessing/TestTargets/#USAF1951>.
80. "Resolution Test Target, Clear Lines on Glass, USAF-1951" (2011), retrieved June 01, 2011, http://search.newport.com/?q=*&x2=sku&q2=RES-1.